

# An Algorithm for the Retrieval of Albedo from Space Using Semiempirical BRDF Models

Wolfgang Lucht, Crystal Barker Schaaf, *Member, IEEE*, and Alan H. Strahler, *Member, IEEE*

**Abstract**—Spectral albedo may be derived from atmospherically corrected, cloud-cleared multiangular reflectance observations through the inversion of a bidirectional reflectance distribution function (BRDF) model and angular integration. This paper outlines an algorithm suitable for this task that makes use of kernel-based BRDF models. Intrinsic land surface albedos are derived, which may be used to derive actual albedo by taking into account the prevailing distribution of diffuse skylight. Spectral-to-broadband conversion is achieved using band-dependent weighting factors. The validation of a suitable BRDF model, the semiempirical Ross–Li (reciprocal RossThick–LiSparse) model and its performance under conditions of sparse angular sampling and noisy reflectances are discussed, showing that the retrievals obtained are generally reliable. The solar-zenith angle dependence of albedo may be parameterized by a simple polynomial that makes it unnecessary for the user to be familiar with the underlying BRDF model. The algorithm given is that used for the production of a BRDF/albedo standard data product from NASA's EOS-MODIS sensor, for which an at-launch status is provided. Finally, the algorithm is demonstrated on combined AVHRR and GOES observations acquired over New England, from which solar zenith angle-dependent albedo maps with a nominal spatial resolution of 1 km are derived in the visible band. The algorithm presented may be employed to derive albedo from space-based multiangular measurements and also serves as a guide for the use of the MODIS BRDF/albedo product.

**Index Terms**—Albedo, bidirectional reflectance distribution function, EOS, MODIS, remote sensing algorithm.

## I. INTRODUCTION

**L**AND surface albedo is one of the most important parameters characterizing the earth's radiative regime and its impact on biospheric and climatic processes [1]–[3]. Albedo is related to land surface reflectance by directional integration and is therefore dependent on the bidirectional reflectance distribution function (BRDF), which describes how the reflectance depends on view and solar angles [4]. Specification of the BRDF provides land surface reflectance explicitly in terms of its spectral, directional, spatial, and temporal characteristics. Fig. 1 illustrates key causes for land surface reflectance anisotropy and the resulting nonlinear relationship between albedo and the reflectance observed by a satellite from a given direction (see [5] and [6] for examples). Albedo quantifies the radiometric inter-

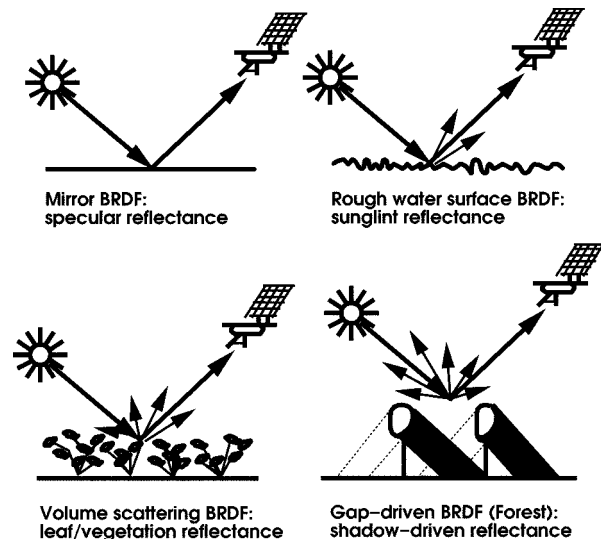


Fig. 1. Basic reasons for land surface reflectance anisotropy: specular scattering such as sunglint, also observed where forward-scattering leaves or soil elements are present, radiative transfer-type volumetric scattering by finite scatterers (leaves of plant canopies) that are uniformly distributed, potentially nonuniformly inclined, which themselves have anisotropic reflectance, and geometric-optical surface scattering, which is given by shadowcasting and mutual obscuration of three-dimensional (3-D) surface elements (for example, of trees in a sparse forest or brushland or of clods on a plowed field or of rock-strewn deserts). In natural systems, all types of scattering are likely to occur simultaneously.

face between the land surface and the atmosphere. On the one hand, it defines the lower boundary for atmospheric radiative transfer [7], [8], while on the other, it details the total shortwave energy input into the biosphere and is a key influence on the surface energy balance [9].

BRDF and albedo have recently received much attention in advanced remote sensing data analysis [10]–[12]. This is due to the fact that the BRDF may be used to standardize reflectance observations with varying sun-view geometries to a common standard geometry [13], [14], a problem frequently encountered in image mosaicking and temporal intercomparisons. The BRDF is also a potential source of biophysical information about the land surface viewed [15]–[17]. Most importantly, however, it allows specification of land surface albedo [18]–[21].

Both BRDF and albedo are determined by land surface structure and optical properties. Surface structure influences the BRDF, for example, by shadowcasting, mutual view shadowing, and the spatial distribution of vegetation elements. Surface optical characteristics determine the BRDF, for example, through vegetation–soil contrasts and the optical attributes of canopy elements. As a consequence, the spatial

Manuscript received December 14, 1998; revised June 29, 1999. This work was supported by NASA, Washington, DC, under Contract NAS5-31369, as part of the EOS-MODIS Project.

W. Lucht was with the Department of Geography and the Center for Remote Sensing, Boston University, Boston, MA 02215. He is now with the Potsdam Institute for Climate Impact Research, Potsdam, Germany.

C. B. Schaaf and A. H. Strahler are with the Department of Geography and the Center for Remote Sensing, Boston University, Boston, MA 02215.

Publisher Item Identifier S 0196-2892(00)02489-X.

and temporal distribution of these land surface properties, as seen in BRDF and albedo features, reflect a variety of natural and human influences on the surface that are of interest to global change research. Such influences on albedo are due to agricultural practices, deforestation and urbanization, the phenological cycle (seasonal dependence and agricultural green-up/harvesting), meteorological parameters (soil wetness and snowfall distribution), and climatological trends (desertification, vegetation cover changes, and snowfall patterns).

Climate models currently employ albedo values derived from the land cover type of each grid box [1]. The underlying albedo tables go back to various field measurements [22], coarse-resolution top-of-atmosphere ERBE observations [23]–[25] or are computed from models [26]. However, there is a need for a more accurate specification of albedo [22], [27] as a function of land cover type, season, and solar zenith angle. This can only be achieved from accurate derivations of kilometer-scale albedo datasets for large areas, allowing the study of the magnitude distribution and of the spatial aggregation of values to coarser resolution for each land cover type and land cover mosaic [28]–[30]. Remote sensing is the most suitable technique for deriving large consistent data sets of land surface parameters [31].

This paper summarizes an algorithm for the derivation of land surface albedo from atmospherically corrected, cloud-cleared, multiangular reflectance observations from space. Symbols are defined in Section II. Section III provides a generic mathematical outline of the algorithm, while Section IV gives a specific realization of the algorithm, especially of the models used. Section V validates the algorithm by investigating in detail the practical properties of all components, especially of the BRDF model. Section VI gives details of an implementation of this algorithm for BRDF/albedo processing of data from NASA's Moderate Resolution Imaging Spectroradiometer (MODIS), providing an at-launch status of this algorithm. It also demonstrates the algorithm on a remotely sensed data set. Section VII summarizes conclusions.

## II. DEFINITIONS

The following is a summary of symbols used in defining the algorithm.

Spectral and directional parameters:

- $\theta$  = solar zenith angle (1)
- $\vartheta$  = view zenith angle (2)
- $\phi$  = view-sun relative azimuth angle (3)
- $\lambda$  = wavelength (4)
- $\Lambda$  = waveband  $\Lambda$  of width  $\Delta\lambda$  (5)

Atmospheric parameters:

- $\tau(\lambda)$  = atmospheric optical depth (6)
- $S(\theta, \tau(\lambda))$  = fraction of diffuse skylight, assumed isotropic (7)
- $D(\theta, \lambda, \tau(\lambda))$  = bottom-of-atmosphere downwelling radiative flux (8)

BRDF-related quantities:

- $\rho(\theta, \vartheta, \phi, \Lambda)$  = an atmospherically corrected observed reflectance (9)

- $R(\theta, \vartheta, \phi, \Lambda)$  = bidirectional reflectance distribution function (BRDF) in waveband  $\Lambda$  (10)

- $K_k(\theta, \vartheta, \phi)$  = BRDF model kernel  $k$  (11)

- $h_k(\theta)$  = integral of BRDF model kernel  $k$  over  $\vartheta$  and  $\phi$  (12)

- $H_k$  = integral of  $h_k(\theta)$  over  $\theta$  (13)

- $f_k(\Lambda)$  = BRDF kernel model parameter  $k$  in waveband  $\Lambda$  (14)

Albedos:

- $a_{bs}(\theta, \lambda)$  = spectral black-sky albedo (15)

- $a_{ws}(\lambda)$  = spectral white-sky albedo (16)

- $a(\theta, \lambda)$  = spectral albedo (17)

- $A(\theta)$  = broadband albedo (18)

Polynomial representations of albedo:

- $P_j(\theta)$  = polynomial expression term  $j$  (19)

- $g_{jk}$  = coefficient  $j$  of a polynomial representation of  $h_k(\theta)$  (20)

- $p_j(\Lambda)$  = coefficient  $j$  of a polynomial representation of  $a_{bs}(\theta, \Lambda)$ , where  $p_j(\Lambda) = \sum_k g_{jk} f_k(\Lambda)$ . (21)

## III. THEORETICAL FRAMEWORK

The following provides a mathematical outline of an algorithm for the derivation of BRDF and albedo from atmospherically corrected multiangular reflectance observations. Reflectance and BRDF are here taken to be of comparable magnitude, which implies neglecting a factor of  $\pi$  in the BRDF as defined by [4].

### A. Kernel-Based BRDF Model and Inversion

The BRDF is expanded into a linear sum of terms (the so-called kernels), characterizing different scattering modes. The superposition assumes that these modes are either spatially distinct within the scene viewed with little cross-coupling, physically distinct within a uniform canopy with negligible interaction, or empirically justified. The resulting BRDF model is called a kernel-based BRDF model [32], [33]:

$$R(\theta, \vartheta, \phi, \Lambda) = \sum_k f_k(\Lambda) K_k(\theta, \vartheta, \phi). \quad (22)$$

Given reflectance observations  $\rho(\Lambda)$  made at angles  $(\theta_l, \vartheta_l, \phi_l)$ , minimization  $\partial c^2 / \partial f_k = 0$  of a least-squares error function

$$c^2(\Lambda) = \frac{1}{d} \sum_l \frac{(\rho(\theta_l, \vartheta_l, \phi_l, \Lambda) - R(\theta_l, \vartheta_l, \phi_l, \Lambda))^2}{w_l(\Lambda)} \quad (23)$$

leads to analytical solutions for the model parameters  $f_k$

$$f_k(\Lambda) = \sum_i \left\{ \sum_j \frac{\rho(\theta_j, \vartheta_j, \phi_j, \Lambda) K_i(\theta_j, \vartheta_j, \phi_j)}{w_j(\Lambda)} \times \left( \sum_l \frac{K_i(\theta_l, \vartheta_l, \phi_l) K_k(\theta_l, \vartheta_l, \phi_l)}{w_l(\Lambda)} \right)^{-1} \right\} \quad (24)$$

where  $w_l(\Lambda)$  is a weight given to each respective observation [e.g.,  $w_l(\Lambda) = 1$  or  $w_l(\Lambda) = \rho(\theta_l, \vartheta_l, \phi_l, \Lambda)$ ], and  $d$  are the degrees of freedom (number of observations minus number of parameters  $f_k$ ). The term in brackets that is to be inverted is the inversion matrix of the linear system, which states the minimization problem. It is interesting to note that this inversion problem can also be formulated in terms of the variances and covariances of the kernel functions, and the covariances of the kernel functions with the observations (cf. [34]).

The fact that a simple BRDF model of this type is linear in its parameters and possesses an analytical solution is a tremendous advantage in large-scale operational data processing and analysis [33], [35]. Other types of BRDF models require numerical procedures that tend to be costly.

### B. Albedo From the BRDF Model

Albedo is defined as the ratio of upwelling to downwelling radiative flux at the surface. Downwelling flux may be written as the sum of a direct component and a diffuse component. Black-sky albedo is defined as albedo in the absence of a diffuse component and is a function of solar zenith angle. White-sky albedo is defined as albedo in the absence of a direct component when the diffuse component is isotropic. It is a constant.

Mathematically, the directional-hemispherical and bi-hemispherical integrals of the BRDF model kernels are defined as

$$h_k(\theta) = \frac{1}{\pi} \int_0^{2\pi} \int_0^{\pi/2} K_k(\theta, \vartheta, \phi) \sin(\vartheta) \cos(\vartheta) d\vartheta d\phi, \quad (25)$$

$$H_k = 2 \int_0^{\pi/2} h_k(\theta) \sin(\theta) \cos(\theta) d\theta. \quad (26)$$

Black-sky and white-sky albedo are then given by

$$a_{bs}(\theta, \Lambda) = \sum_k f_k(\Lambda) h_k(\theta), \quad (27)$$

$$a_{ws}(\Lambda) = \sum_k f_k(\Lambda) H_k. \quad (28)$$

Note that the kernel integrals  $h_k(\theta)$  and  $H_k$  do not depend on the observations and may therefore be precomputed and stored. This is a feature specific to kernel-based BRDF models.

### C. Basic Polynomial Representation of Albedo

Given model parameters  $f_k$  retrieved from multiangular reflectance observations, albedo is given by integrals of the BRDF model. Since analytical expressions for these integrals are most likely not available, they have to be tabulated. However, in many circumstances a simple analytical expression is preferable. Since the directional dependence of albedo is much

less complex than that of the BRDF, a simple parameterization by polynomials of the solar zenith angle should suffice

$$h_k(\theta) = \sum_j g_{jk} P_j(\theta), \quad (29)$$

$$\begin{aligned} a_{bs}(\theta, \Lambda) &= \sum_k f_k(\Lambda) \sum_j g_{jk} P_j(\theta) \\ &= \sum_j p_j(\Lambda) P_j(\theta). \end{aligned} \quad (30)$$

Due to the linearity of the BRDF model, there is a linear relationship between the polynomial coefficients for the kernel integrals and those for the black-sky albedo

$$p_j(\Lambda) = \sum_k g_{jk} f_k(\Lambda). \quad (31)$$

This allows us to link the polynomial representation of individual kernel integrals to that of a specific albedo function.

### D. Atmospheric Effects

Black-sky albedo and white-sky albedo mark the extreme cases of completely direct and completely diffuse illumination. Actual albedo is a value interpolated between these two depending on the aerosol optical depth  $\tau$ . If diffuse skylight is assumed to be an isotropic fraction  $S(\tau)$  of total illumination, then [36]

$$\begin{aligned} a(\theta, \Lambda) &= \{1 - S(\theta, \tau(\Lambda))\} a_{bs}(\theta, \Lambda) \\ &\quad + S(\theta, \tau(\Lambda)) a_{ws}(\Lambda) \end{aligned} \quad (32)$$

$$\begin{aligned} &= \sum_k \sum_j \{1 - S(\theta, \tau(\Lambda))\} g_{jk} f_k(\Lambda) P_j(\theta) \\ &\quad + S(\theta, \tau(\Lambda)) f_k(\Lambda) H_k \end{aligned} \quad (33)$$

where

|                                      |   |
|--------------------------------------|---|
| $f_k(\Lambda)$                       | from BRDF observations;   |
| $H_k, P_j(\theta)$ ,<br>and $g_{jk}$ | known precomputed mathematical quantities independent of the surface observations and the atmosphere; |
| $S(\theta, \tau(\Lambda))$           | atmospheric state.  |

### E. Spectral-to-Broadband Albedo Conversion

Earth-scanning remote sensing instruments generally acquire data in narrow spectral bands. However, the total energy reflected by the Earth's surface in the shortwave domain is characterized by the shortwave (0.3–5.0  $\mu\text{m}$ ) broadband albedo. Frequently, the visible (0.3–0.7  $\mu\text{m}$ ) and near-infrared (0.7–5.0  $\mu\text{m}$ ) broadband albedos are also of interest due to the marked difference of the reflectance of vegetation in these two spectral regions.

Spectral-to-broadband conversion may proceed in two steps. The first is a spectral interpolation and extrapolation

$$a(\theta, \lambda) = F(a(\theta, \Lambda)) \quad (34)$$

where  $F$  is a function or procedure supplying albedo at any wavelength in the broadband range based on the given spectral values. This function may, for example, be a splining function with adequately chosen tie-down points at either end of the range or a typical spectrum characterizing the scene type that is fitted to the observed spectral albedos.

The second step is then the conversion of spectral albedo  $a(\theta, \lambda)$  to broadband albedo  $A(\theta)$ . The latter is defined as the ratio of broadband upwelling radiative flux  $U_{BB}$  to broadband downwelling flux  $D_{BB}$ . Since  $U_{BB} = \int U(\lambda) d\lambda$ ,  $D_{BB} = \int D(\lambda) d\lambda$ , and in the first of these  $U(\lambda) = a(\lambda)D(\lambda)$ , which is the spectral definition of albedo, it follows that spectral albedo is related to broadband albedo through spectral integration weighted by the bottom-of-atmosphere downwelling spectral solar flux  $D$

$$A(\theta) = \frac{\int_{\lambda_1}^{\lambda_2} a(\theta, \lambda) D(\theta, \lambda, \tau(\lambda)) d\lambda}{\int_{\lambda_1}^{\lambda_2} D(\theta, \lambda, \tau(\lambda)) d\lambda}. \quad (35)$$

Since  $D$  is dependent on atmospheric state, broadband albedo is also dependent on atmospheric state in addition to the dependence of spectral albedo upon the diffuse skylight. If a standard atmosphere with given  $\tau(\lambda)$  is assumed to represent a typical situation, the two steps may be combined by determining empirical conversion coefficients  $c_i$  that directly convert narrowband spectral albedos into broadband albedos

$$A(\theta) = \sum_i c_i a(\theta, \Lambda_i) \quad (36)$$

where  $c_i$  are appropriately chosen weights reflecting the distribution of downwelling radiative flux with respect to the location of the available spectral bands. They may be empirically determined from computer simulation [37].

#### IV. ALGORITHM DETAILS

Following the outline given, what is required for deriving albedo from satellite observations are realizations of the following:

- 1) multiangular reflectance observations that are atmospherically corrected;
- 2) a kernel-driven BRDF model;
- 3) the polynomial representation  $h_k(\theta) = \sum_j p_j P_j(\theta)$  for each BRDF kernel;
- 4) a simple model relating  $S$  to  $\tau$  as a function of wavelength  $\lambda$ ;
- 5) the interpolation function spectral-to-broadband  $F$  and some representation of downwelling flux  $D(\theta, \lambda, \tau(\lambda))$  or conversion coefficients  $c_i$  for a given atmosphere.

##### A. Ross-Li BRDF Model

A BRDF model is required for deriving albedo from multiangular reflectance observations. Several models of the form given by (22) are available. The modified Walthall model [19], [38] is an empirical, kernel-driven model with simple trigonometric expressions as kernels. The model by Roujean *et al.* [32] and those by Wanner *et al.* [33] are semiempirical. The kernels in these models are derived from more complex physical theory through simplifying assumptions and approximations. Since these models provide a simple parameterization of an otherwise potentially complicated function, they sometimes are also called parametric models.

The theoretical basis of these semiempirical models is that the land surface reflectance is modeled as a sum of three ker-

nels representing basic scattering types: isotropic scattering, radiative transfer-type volumetric scattering as from horizontally homogeneous leaf canopies, and geometric-optical surface scattering as from scenes containing 3-D objects that cast shadows and are mutually obscured from view at off-nadir angles. Equation (22) then takes on the specific form given by Roujean *et al.* [32],

$$R(\theta, \vartheta, \phi, \Lambda) = f_{iso}(\Lambda) + f_{vol}(\Lambda) K_{vol}(\theta, \vartheta, \phi) + f_{geo}(\Lambda) K_{geo}(\theta, \vartheta, \phi). \quad (37)$$

One may think of the volume-scattering term as expressing effects caused by the small (interleaf) gaps in a canopy, whereas the geometric-optical term expresses effects caused by the larger (intercrown) gaps.

A suitable expression for  $K_{vol}$  was derived by Roujean *et al.* [32]. It is called the RossThick kernel, for its assumption of a dense leaf canopy. It is a single-scattering approximation of radiative transfer theory by Ross [39] consisting of a layer of small scatterers with uniform leaf angle distribution, a Lambertian background, and equal leaf transmittance and reflectance. Its form, normalized to zero for  $\theta = 0$ ,  $\vartheta = 0$ , and writing the phase angle as  $\cos \xi = \cos \theta \cos \vartheta + \sin \theta \sin \vartheta \cos \phi$ , is

$$K_{vol} = K_{RT} = \frac{(\pi/2 - \xi) \cos \xi + \sin \xi}{\cos \theta + \cos \vartheta} - \frac{\pi}{4}. \quad (38)$$

A suitable expression for  $K_{geo}$  that has been found to work well with observed data was derived by Wanner *et al.* [33]. It is called the LiSparse kernel for its assumption of a sparse ensemble of surface objects casting shadows on the background, which is assumed Lambertian. The kernel is derived from the geometric-optical mutual shadowing BRDF model by Li and Strahler [40]. It is given by the proportions of sunlit and shaded scene components in a scene consisting of randomly located spheroids of height-to-center-of-crown  $h$  and crown vertical-to-horizontal radius ratio  $b/r$ . The original form of this kernel is not reciprocal in  $\theta$  and  $\vartheta$ , a property that is approximately expected from homogeneous natural surfaces viewed at coarse spatial scale. The main reason for this nonreciprocity is that the scene component reflectances are assumed to be constants independent of solar zenith angle. If the sunlit component is simply assumed to vary as  $1/\cos \theta$ , the kernel takes on the reciprocal form given here, to be called LiSparse-R

$$K_{geo} = k_{LSR} = O(\theta, \vartheta, \phi) - \sec \theta' - \sec \vartheta' + \frac{1}{2} (1 + \cos \xi') \sec \theta' \sec \vartheta' \quad (39)$$

where

$$O = \frac{1}{\pi} (t - \sin t \cos t) (\sec \theta' + \sec \vartheta'), \quad (40)$$

$$\cos t = \frac{h}{b} \frac{\sqrt{D^2 + (\tan \theta' \tan \vartheta' \sin \phi)^2}}{\sec \theta' + \sec \vartheta'} \quad (41)$$

$$D = \sqrt{\tan^2 \theta' + \tan^2 \vartheta' - 2 \tan \theta' \tan \vartheta' \cos \phi} \quad (42)$$

$$\cos \xi' = \cos \theta' \cos \vartheta' + \sin \theta' \sin \vartheta' \cos \phi, \quad (43)$$

$$\theta' = \tan^{-1} \left( \frac{b}{r} \tan \theta \right) \text{ and } \vartheta' = \tan^{-1} \left( \frac{b}{r} \tan \vartheta \right). \quad (44)$$

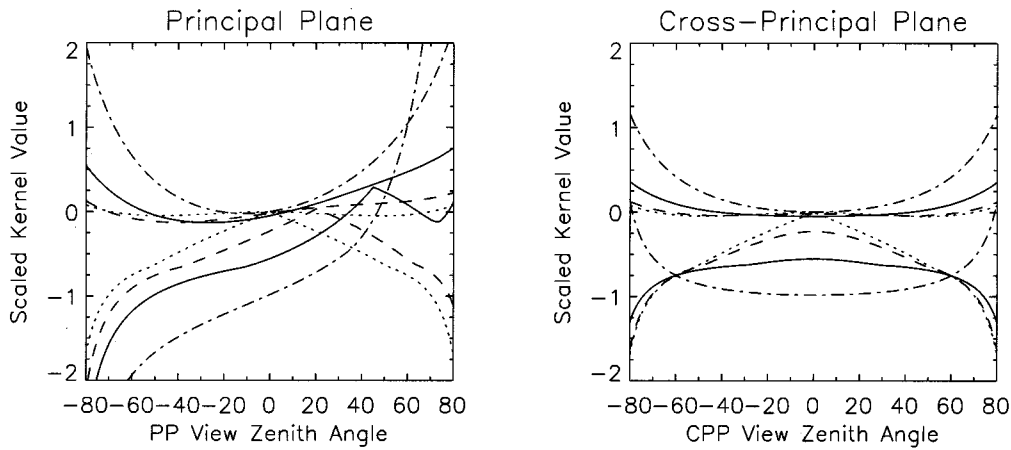


Fig. 2. Principal plane and cross-principle solar plane plots of the RossThick (upper curves) and LiSparse-R (lower curves) BRDF model kernel values (arbitrary units; the LiSparse-R kernel values were divided by 2 for better plotting). The sun is located at positive zenith angles of 0° (dotted lines), 20° (dashed lines), 45° (solid lines), and 70° (dashed-dotted line) solar zenith angle. The parameter  $h/b$  of the LiSparse-R kernel was set to 2.0 and the parameter  $b/r$  to 1.0.

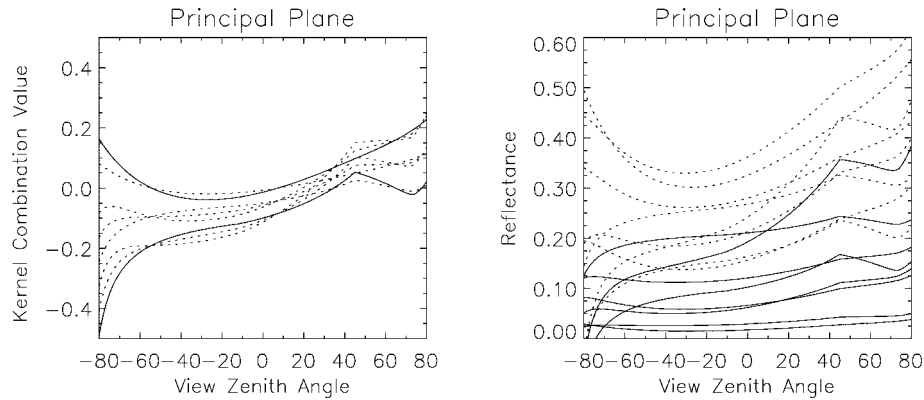


Fig. 3. BRDF shapes which the Ross-Li BRDF model acquires under natural conditions on the principal solar plane for a solar zenith angle of 45°. Left panel: shape of the BRDF using typical values for the model parameters. The two solid lines represent the maximal volume scattering and geometric-optical scattering found for 18 field-observed BRDF's representing a wide range of barren and vegetated cover types in the red and near-infrared wavebands. The dotted lines are intermediate cases where the parameters take on either their respective maximal value, half of it, or are zero in all possible combinations. Right panel: shape of the BRDF using observed model parameters in the red (solid lines) and near-infrared (dotted lines) wavebands. The datasets used represent sparse brushland, dense broadleaf forest, dense barren trees on snow, dense needleleaf forest, sparse grass, dense grassland, and barren soil (data collected by numerous investigators).

Here,  $O$  is the overlap area between the view and solar shadows. The term  $\cos t$  should be constrained to the range  $[-1, 1]$ , as values outside of this range imply no overlap and should be disregarded. Note that the dimensionless crown relative height and shape parameters  $h/b$  and  $b/r$  are within the kernel and should therefore be preselected. For MODIS processing and the examples given in this paper,  $h/b = 2$  and  $b/r = 1$  (i.e., the spherical crowns are separated from the ground by half their diameter). Generally, the shape of the crowns affect the BRDF more than their relative height [33].

Full derivations of the RossThick and the LiSparse kernels can be found in Wanner *et al.* [33]. The combination of the RossThick with the LiSparse-R kernel has been called the RossThick-LiSparse-R model, but will here be simply referred to as the Ross-Li BRDF model, as it is the standard model to be used in MODIS BRDF processing. Fig. 2 shows the shapes of these kernels for different solar zenith angles, and Fig. 3 shows the shape of the resulting BRDF when using realistic model parameters taken from BRDF datasets observed in the field over a variety of land cover types. Note that the behavior of the two kernels is different in nature over large angular

ranges. While they are not perfectly orthogonal functions, as would be ideal for the inversion process, they are sufficiently independent to allow stable recovery of the parameters for many angular sampling distributions. The absence of excessive kernel-to-kernel correlation is key to reliable inversions.

When deriving the model parameters  $f_k$  by minimization of the error term  $e^2$ , care should be taken that the resulting model parameters are not negative. This is required from physical considerations and in order to maintain the semiorthogonality of the scattering kernels. If the mathematical inversion produces a negative parameter, the next best valid value for this parameter is zero, under which imposed condition, the remaining kernel parameters should be rederived [35].

### B. Ross-Li Polynomial Albedo Representation

The solar zenith angle dependence of the black-sky albedo integrals  $h_k(\theta)$  of the RossThick and LiSparse-R kernels are relatively benign functions, shown in Fig. 4. Therefore, a simple mathematical expression may be found to express these functions. Such a representation may be more convenient in land

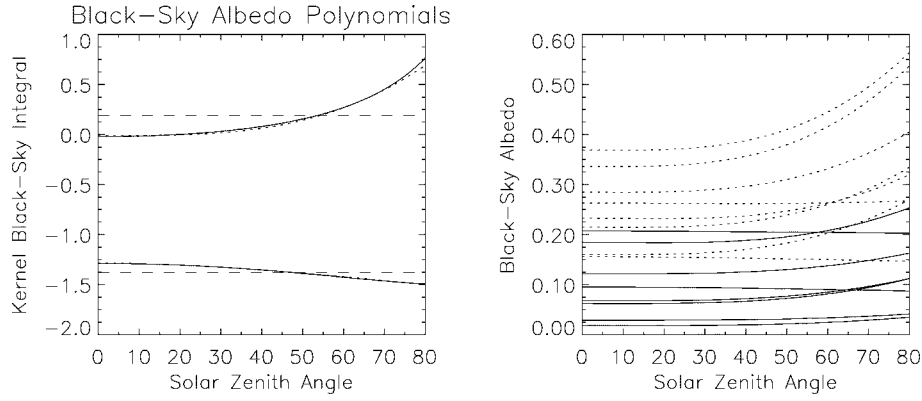


Fig. 4. Solar zenith angle dependence, which the Ross-Li BRDF model produces. Left panel: black-sky integral values of the RossThick and of the LiSparse-R kernel (solid lines) and their polynomial representations (dotted lines). Results are nearly indistinguishable. Also shown is the value of the white-sky albedo as a constant for each kernel (dashed lines). Right panel: black-sky albedo using observed model parameters in the red (solid lines) and near-infrared (dotted lines) wavebands. The datasets used are the same as those in Fig. 3 and represent sparse brushland, dense broadleaf forest, dense barren trees on snow, dense needleleaf forest, sparse grass, dense grassland, and barren soil (data collected by numerous investigators).

surface modeling than using a look-up table of the kernel integrals. In either case, the linear nature of kernel-driven BRDF models has the great advantage of allowing either the look-up table or, alternately, the coefficients of the simple mathematical expression, to be predetermined. This is not the case for non-linear BRDF models, where they have to be recomputed after each inversion.

Several hundred three-term expressions involving  $\theta$ ,  $\cos(\theta)$ ,  $\sin(\theta)$ , their squares, and various forms of products of these terms were investigated with respect to their ability to provide a simple functional representation of the kernel integrals, and hence, of black-sky albedo. It was found that expressions containing  $g_{0k} + g_{1k}\theta^2$  provided very good fits to kernels  $K$ . The third term may take on various forms, but simply using  $g_{2k}\theta^3$  provides nearly as good a fit and provides a simple polynomial representation. The chi-square of fitting

$$h_k(\theta) = g_{0k} + g_{1k}\theta^2 + g_{2k}\theta^3 \quad (45)$$

to numerically computed integrals of the kernels as a function of solar zenith angle is found to be only 0.013. Table I gives the coefficients found. Fig. 4 shows that the polynomial representation of the black-sky integrals of the RossThick and the LiSparse-R kernel are nearly perfect up to  $80^\circ$ . For the LiSparse-R kernel, the fit actually is excellent to nearly  $90^\circ$ , and for the RossThick kernel it yields somewhat lower values between  $80$ – $90^\circ$ . The latter characteristic may actually be advantageous because projections of the form  $1/\cos(\theta)$ , which is common in simple BRDF models, are increasingly unrealistic at large angles, and yield values that are too large as  $90^\circ$  zenith angle is approached. Generally, the BRDF model results at angles larger than  $80^\circ$  should be viewed with suspicion. Luckily, the term  $\sin(\theta)\cos(\theta)$  in the white-sky albedo integral ensures that this slight problem has no effect on the calculation of the diffuse albedo.

Spectral black-sky albedo then is given by

$$\alpha_{bs}(\theta, \Lambda) = f_{iso}(\Lambda) (g_{0iso} + g_{1iso}\theta^2 + g_{2iso}\theta^3) + f_{vol}(\Lambda) (g_{0vol} + g_{1vol}\theta^2 + g_{2vol}\theta^3) + f_{geo}(\Lambda) (g_{0geo} + g_{1geo}\theta^2 + g_{2geo}\theta^3). \quad (46)$$

TABLE I  
COEFFICIENTS FOR THE POLYNOMIAL  
 $h_k(\theta) = g_{0k} + g_{1k}\theta^2 + g_{2k}\theta^3$

| Term $g_{jk}$<br>for kernel $k$ | $k =$<br>Isotropic | $k =$<br>RossThick | $k =$<br>LiSparse-R |
|---------------------------------|--------------------|--------------------|---------------------|
| $g_{0k}$ (term 1)               | 1.0                | -0.007574          | -1.284909           |
| $g_{1k}$ (term $\theta^2$ )     | 0.0                | -0.070987          | -0.166314           |
| $g_{2k}$ (term $\theta^3$ )     | 0.0                | 0.307588           | 0.041840            |
| white-sky integral              | 1.0                | 0.189184           | -1.377622           |

Using  $\theta^4$  as a final term gives a slight but not significant improvement.

A comparison of results from the exact calculation with results from the polynomial for several diverse field-measured BRDF data sets shows that for solar zenith angles less than  $80^\circ$ , the angle-averaged error made is less than 1% relative in both the red and the near-infrared bands, and between 1–2% relative when taking into account all solar zenith angles up to  $90^\circ$ .

### C. Atmospheric Effects

The influence of diffuse skylight on the albedo may be taken into account by interpolating between black-sky and white-sky albedo as a function of the fraction of diffuse skylight [36], which is a function of aerosol optical depth. The underlying assumption of an isotropic distribution of the diffuse skylight is approximate but avoids the expense of an exact calculation while capturing the major part of the phenomenon [41]. Fig. 4 shows the difference between the black-sky and white-sky integrals of the RossThick and LiSparse-R kernels, which at solar zenith angles around  $45^\circ$  is not very large. In this angular range albedo is nearly independent of atmospheric conditions. Fig. 5 demonstrates this difference as computed from the BRDF model fitted to multiangular reflectances observed for a dense deciduous forest. For comparison, interpolated albedo including diffuse skylight is shown for different optical depths.

The magnitude of the diffuse skylight fraction  $S(\theta)$  required for this interpolation is demonstrated for the red and near-infrared bands and for different values of the aerosol optical depth

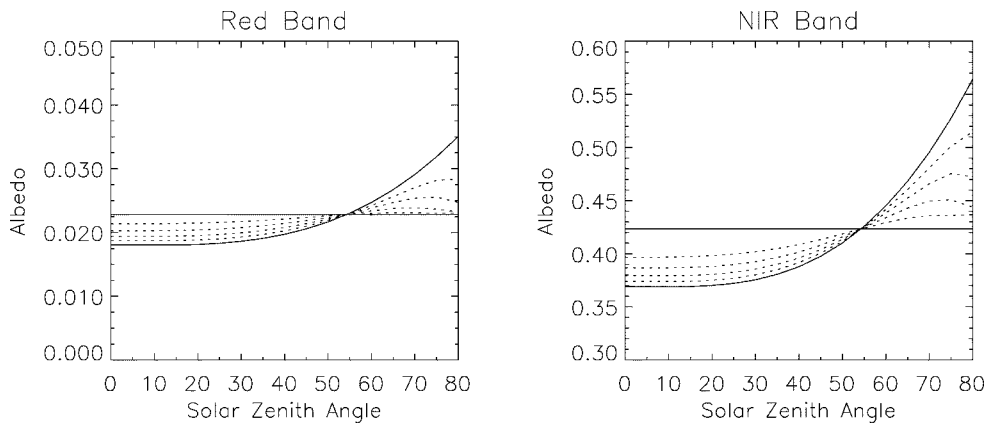


Fig. 5. Albedo (dotted lines) as an interpolation between black-sky (curved solid line) and white-sky albedo (constant solid line) as a function of the fraction of diffuse skylight, calculated from the aerosol optical depth at 550 nm. A continental aerosol model and a U.S. standard 62 atmosphere were used in the 6S atmospheric radiative transfer simulation code. Aerosol optical depths at 550 nm are (dotted curves from bottom to top): 0.2, 0.5, 1.0, and 2.0, corresponding to conditions of increasing haziness. The BRDF used is that of a deciduous forest.

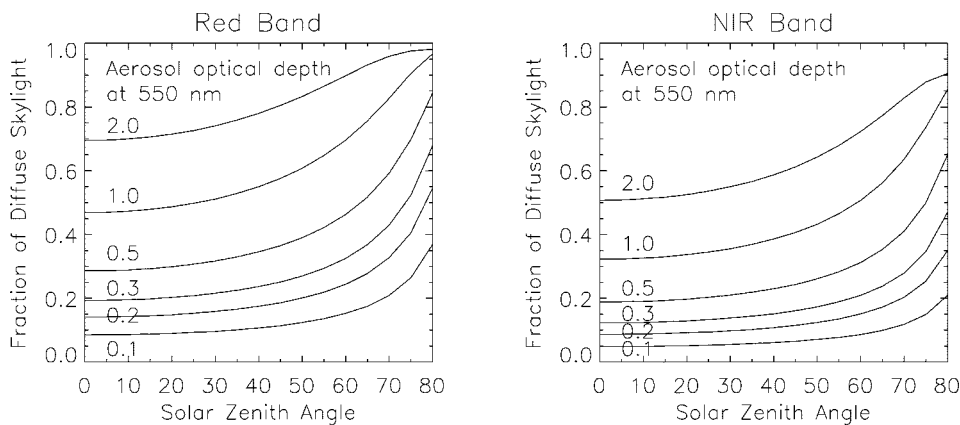


Fig. 6. Solar zenith angle dependence of the fraction of diffuse skylight in the red and the near-infrared band as a function of aerosol optical depth at 550 nm. A continental aerosol model and a U.S. standard 62 atmosphere were used in the 6S atmospheric radiative transfer simulation code. This fraction may be used to interpolate between the black-sky albedo and the white-sky albedo to approximate albedo under clear, hazy, and cloudy skies. Aerosol optical depths at 550 nm are (curves from bottom to top): 0.1, 0.2, 0.3, 0.5, 1.0, and 2.0.

at 550 nm in Fig. 6. The 6S atmospheric radiative transfer simulation code [42] was run as a function of solar zenith angle in the MODIS red and near-infrared bands. The continental aerosol model and a U.S. standard 62 atmosphere were specified.

There is a possibility [43], [44] that the fraction of diffuse to total irradiation may be parameterized in a relatively simple way at least for moderate solar zenith angles. This parameterization seems to be relatively reliable in the visible domain, which is the domain contributing most to broadband albedo and could lead to a further simplification of the current algorithm through additional parameterization.

#### D. Spectral-to-Broadband Albedo Conversion

Spectral-to-broadband conversion is based on the sparse angular sampling that satellite sensors like MODIS, the Multiangle Imaging Spectrometer (MISR), polarization and directionality of Earth reflectances (POLDER), medium resolution imaging spectrometer (MERIS), or the Advanced Very High Resolution Spectrometer (AVHRR) provide. The MODIS sensor has seven discrete shortwave bands, three in the visible and four in the infrared [45]. MISR also provides three visible bands but has only

one band in the near-infrared [46]. MERIS has programmable bands in the visible and near-infrared. The AVHRR sensor provides only the red band for estimation of the visible and the near-infrared band for estimation of the near-infrared broadband albedo [47].

Various studies in the published literature suggest spectral-to-broadband conversion coefficients that allow to estimate broadband albedos from such spectrally sparse observations. Liang *et al.* [37] used observed spectra and numerical simulations to produce conversion coefficients for MODIS and MISR. Several authors provide conversion coefficients for the AVHRR (e.g., [48]–[50]). Of these, we found the coefficients given by Brest and Goward [51] to be reliable even though they were derived for working with Landsat TM data. Coefficients are listed in Table II, results demonstrating their potential and errors incurred for typical cases are presented later.

One should keep in mind that spectral-to-broadband conversion is a function of atmospheric state to the extent that the spectral distribution of the solar downwelling flux depends on atmospheric properties and the solar zenith angle. The conversion coefficients listed in Table II are derived for typical average cases. Variations of the exact results with aerosol optical depth

TABLE II  
SPECTRAL-TO-BROADBAND CONVERSION COEFFICIENTS

| Band  | Wavelength  | VIS-BB         | NIR-BB  | SW-BB   |
|---|-------------|----------------|---------|---------|
| <i>MODIS (from Liang et al. [37])</i>             |             |                |         |         |
| Blue  | 0.459–0.479 | 0.4364         | 0.0000  | 0.3489  |
| Green   | 0.545–0.565 | 0.2366         | 0.0000  | –0.2655 |
| Red   | 0.620–0.670 | 0.3265         | 0.0000  | 0.3973  |
| NIR   | 0.841–0.876 | 0.0000         | 0.5447  | 0.2382  |
| 1.2   | 1.230–1.250 | 0.0000         | 0.1363  | 0.1604  |
| 1.6   | 1.628–1.652 | 0.0000         | 0.0469  | –0.0138 |
| 2.1   | 2.105–2.155 | 0.0000         | 0.2536  | 0.0682  |
| Intercept   |             | –0.0019        | –0.0068 | 0.0036  |
| <i>MISR (from Liang et al. [37])</i>              |             |                |         |         |
| Blue  | 0.426–0.467 | 0.3511         | 0.000   | 0.1587  |
| Green   | 0.544–0.571 | 0.3923         | 0.000   | –0.2463 |
| Red   | 0.662–0.682 | 0.2603         | 0.000   | 0.5442  |
| NIR   | 0.847–0.886 | 0.0000         | 0.6088  | 0.3748  |
| Intercept   |             | –0.0030        | 0.1442  | 0.0149  |
| <i>AVHRR (for TM, from Brest and Goward [51])</i> |             |                |         |         |
| Red   | 0.580–0.680 |                |         | 0.526   |
| NIR   | 0.725–1.100 | vegetated:     |         | 0.418   |
| NIR   | 0.725–1.100 | non-vegetated: |         | 0.474   |
| NIR   | 0.725–1.100 | snow and ice:  |         | 0.321   |

and solar zenith angle are small but affect retrieval accuracies on the level of a few percent.

## V. ALGORITHM VALIDATION

### A. Ross–Li BRDF Model Validation

A basic requirement of the BRDF model to be used is that it be capable of representing accurately the shapes of naturally occurring BRDF's. Earlier work using various forms of kernel-based models already has demonstrated the feasibility of this approach in BRDF modeling [32], [52], [53]. These works show that kernel-based models give reasonable fits to field-measured BRDF data sets in the sense that they reproduce with their three parameters all the major features of the BRDF for a wide variety of situations including barren and densely vegetated cases.

In order to specifically study the Ross–Li model used here, a set of 61 very diverse field-measured BRDF data sets was assembled. These cover all major types of landcover, such as dense and sparse broadleaf and grasslike crops of various types on bright and dark soils, needleleaf and broadleaf forests, including situations with snow backgrounds and barren trees, tundra, desert, snow, dark and bright barren soils, etc. A

majority of these data sets were acquired using the Portable Apparatus for Rapid Acquisition of Bidirectional Observations of Land and Atmosphere (PARABOLA) instrument by Deering and coworkers [54]–[56], but others are included as well. These latter datasets are mostly ground-based observations as well (for example, those by Kimes and coworkers [57]–[59]) but also include some acquired from the air. The total of 61 datasets may not be completely representative in terms of the distribution of types but gives an indication of model performance based on the current state of BRDF field observation. Most sets have excellent coverage of the viewing hemisphere at several different solar zenith angles. Only a few sets are sparse.

Each of the 61 data sets was inverted for all available viewing and solar zenith angles simultaneously using the Ross–Li BRDF model. The residual deviation between modeled and observed reflectances, the RMSE, was expressed as a fraction of the typical reflectance, here represented by the white-sky albedo as predicted by the model. The average RMSE was 20% of the white-sky albedo in the red and 15% in the near-infrared band. The median values were 16 and 13%, respectively. These errors include artifacts and inconsistencies in the field data. For example, some data sets as measured display an irregular variability of the reflectance at some angles that may be due to the difficulty of the measurement. This variability will naturally contribute to the RMSE found in inversion.

The results found for the Ross–Li model are almost identical to those for other well-established semiempirical BRDF models. The nonreciprocal original RossThick–LiSparse BRDF model [33], the RossThick–Roujean model [32], the modified Walthall model [19], [38], and the modified Rahman model [60] all have red band average RMSE's of between 19–21% of the white-sky albedo (14–18% in the median), and average near-infrared band RMSE's between 14–16% of the white-sky albedo (11–14% in the median).

Histograms of the RMSE look very similar for all of the models. Fig. 7 shows the accumulative percentage of datasets with RMSE's below a given threshold. All four semiempirical BRDF models studied, which all use three parameters to model the BRDF and the empirical model, show a very similar behavior. Where one model has difficulties representing the observed BRDF in all its complexity, others generally have the same problem. This may be due to similar deficiencies of each model or peculiarities in the field data.

The RMSE's found are not all as small as one would like, but to the extent that a simple three-parameter general inversion model can be expected to model the complexities of a great variety of BRDF datasets acquired in the field, they are satisfactory. Visual inspection of reflectance plots shows that the basic multidirectional anisotropy of very different land surfaces may be adequately modeled, even though details like the behavior at large zenith angles or in the hotspot region may be represented less accurately. Improved models with a relative RMSE below 10% in all cases would be much desired in the near future.

Even though the models are very similar in their ability to fit field-observed BRDF's when well constrained by observations, they display different abilities to predict the BRDF and albedo from sparse angular sampling or noisy data. For example, the empirical modified Walthall model is less reliable in this respect



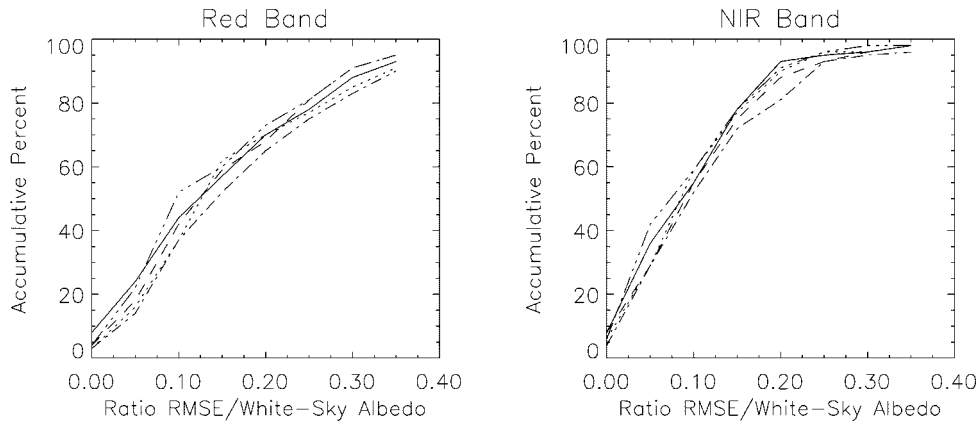


Fig. 7. Inversion root mean square errors (RMSE's) as a fraction of predicted white-sky albedo for 61 different field-observed BRDF datasets inverted using four different semiempirical BRDF models and the empirical model in the red and near-infrared bands. The BRDF datasets used are from a wide variety of sources and represent all major landcover types (crops, grasses, forests, and barren surfaces) with a variety of soil brightnesses, plant densities, and types, including snow backgrounds. The five BRDF models are the Ross-Li model (solid line), the nonreciprocal RossThick-LiSparse model (dashed line), the RossThick-Roujean model (dashed-dotted line), the modified Walthall model (dotted line), and the modified Rahman model (triple dotted-dashed line). The plots show that all of these models fit the 61 field-observed data sets with similar errors. Note that the error shown also includes possible inconsistencies and irregularities in the field observations themselves.

due to its lack of a semiphsical basis [61]. For the Ross-Li BRDF model, these issues are addressed in Section VI.

#### B. Inversion Accuracy with Sparse Angular Sampling

Even if a BRDF model is able to represent land surface BRDF's sufficiently well under conditions of good angular sampling, it is important to investigate whether the retrievals remain stable when angular sampling is sparse, as is the case from space-based satellite sensors. The achievable accuracy will depend not only on the number of observations but also on their angular distribution, that is, on sensor scan pattern and orbit, latitude, and solar zenith angle. Reflectance and albedo retrieval accuracies under sparse angular sampling were investigated for kernel-driven models by Privette *et al.* [62] and Lucht [61]. The former paper relied on field-observed BRDF's that were systematically sampled sparsely. Ten different simple BRDF models were tested. The latter paper used a discrete ordinates radiative transfer code by Myneni *et al.* [63] to generate synthetic reflectances for the exact MODIS and MISR observation geometries throughout the year.

The first study [62] did not include the Ross-Li BRDF model but used its nonreciprocal version, which is very similar at most angles. It concluded that this model was one of two models that performed best overall. The second study [61] did use the Ross-Li model. The detailed results found for albedo and reflectance inversion accuracies are summarized in Table III. The first is for cloudfree conditions, indicating the achievable accuracies under optimal sampling conditions. The second investigates the accuracies found when half of the observations are lost due to clouds. This last condition does not apply to the MISR instrument, which acquires the multiangular observations instantaneously and therefore generally provides either all views or none.

The analysis was carried out for MODIS and for MISR angular sampling as well as for combined sampling for six different surface types, the red and the near-infrared bands, observations geometries throughout the year and at different latitudes from pole to pole. The sampling period was 16 days. Median

TABLE III  
ALBEDO RETRIEVAL ACCURACIES (MEDIAN AND RANGE, PERCENT RELATIVE) (AFTER LUCHT [61]; EXPANDED)

| Sensor(s), Cloudiness                 | Red Band       | NIR Band       |
|---------------------------------------|----------------|----------------|
| At solar zenith angle of observations |                |                |
| MODIS 0%                              | 5.5 (2.7–10.6) | 3.5 (1.4–5.3)  |
| MISR 0%                               | 4.1 (2.1–10.7) | 2.4 (1.0–5.5)  |
| MODIS+MISR 0%                         | 4.4 (0.7–10.1) | 2.0 (0.8–4.9)  |
| MODIS 50%                             | 7.7 (1.6–13.0) | 4.5 (0.7–8.1)  |
| MISR 50%                              | n/a            | n/a            |
| MODIS+MISR 50%                        | 4.1 (1.6–10.1) | 2.3 (0.7–5.4)  |
| At other solar zenith angles          |                |                |
| MODIS 0%                              | 7.6 (1.9–19.6) | 3.5 (1.2–19.0) |
| MISR 0%                               | 5.6 (1.3–19.2) | 3.0 (0.9–12.0) |
| MODIS+MISR 0%                         | 5.5 (1.3–18.4) | 2.4 (0.8–13.1) |
| MODIS 50%                             | 9.5 (2.3–22.2) | 6.7 (0.9–19.5) |
| MISR 50%                              | n/a            | n/a            |
| MODIS+MISR 50%                        | 5.7 (1.6–18.6) | 4.5 (0.8–13.9) |

accuracies and ranges encompassing two thirds of all values are listed for retrievals of black-sky albedo at the respective mean solar zenith angle of the observations (which varies with latitude and time of year) and for other solar zenith angles (i.e., 0, 30, and 60°, and for the white-sky albedo, irrespective of the solar zenith angle of observation). The latter poses a very severe test, as albedo is retrieved at solar zenith angles that are potentially far from the angles sampled. For example, at high latitudes the solar zenith angle of the observations may have been 70°, but the accuracy of correctly predicting albedo is also investigated

for a nadir solar zenith angle. Even though the sun will never be at nadir at the extreme latitude of this example, the reflective properties of the surface at such angles still play a role under diffuse illumination conditions, for example an overcast sky.

Table III reveals that retrievals generally achieve accuracies within 10% in the red band with a median error of around 5%. These percentages are relative to the true albedo. In the near-infrared band, retrievals are accurate to within 5%, with a median of about 3%. Cloudiness does not severely affect the retrieval accuracy of combined MODIS and MISR sampling as long as the angular distribution of the samples lost to clouds is relatively random. Cloudiness increases errors by several percent if only MODIS angular sampling is used.

At solar zenith angles extrapolated freely away from that of the observation, the errors are somewhat larger, as expected. Median errors in the red band are around 8%, with worst cases producing errors of up to 20%. In the near-infrared band, the median error is about 4%, also with 20% errors possible in the worst cases. Given the angular sampling available from the sensors, and the very severe test these extrapolations pose, these are very satisfactory results. In a typical case, albedo at any solar zenith angle will be retrieved to within 10% relative. This accuracy should be a great improvement over other techniques for determining albedo which do not explicitly take into account the bidirectional effects of the surface.

The accuracy found for angular sampling provided by MODIS alone should be comparable to that provided by AVHRR or by MERIS. The combined sampling of MODIS and MISR is not quite as good as that achieved by POLDER over several orbits. The paper by Lucht [61] gives more detailed results and also investigates the accuracy with which BRDF-corrected nadir reflectance, of importance for BRDF-normalization of images or vegetation indices, is retrieved at different solar zenith angles.

### C. Noise Sensitivity

When multiangular observations from different orbits are assembled over a period of time to provide a varied angular sampling for BRDF model inversion, as is required for observations from MODIS, MERIS, or the AVHRR, a certain amount of noise-like variation may be expected in the data. This is due to slight changes in surface moisture, atmospheric conditions, geolocation, footprint size, etc., from one orbit to the next.

The sensitivity to noise of reflectance and albedo retrieval using the nonreciprocal RossThick-LiSparse kernel-driven BRDF models was investigated systematically by Lucht and Lewis [64]. Results were found to be very similar for different kernel-based models so that they are also relevant for the reciprocal Ross-Li BRDF model. So-called weights of determinations, or noise sensitivity factors, are derived analytically from an analysis of the matrix inverting the kernel-driven BRDF model [see (24)]. These factors specify the level of noise expected in a given computed linear function of the model parameters (such as the model parameters, reflectance, or albedo) as a fraction of the noise in the observed reflectances, which is estimated to be equal to the RMSE. Values less than unity indicate a suppression of noise in the retrieval, factors larger than unity an increase. Noise sensitivity factors are

TABLE IV  
NOISE SENSITIVITY FACTORS (MEDIAN AND RANGE) (AFTER LUCHT AND LEWIS [64]; EXPANDED)

| Sensor(s), Cloudiness                 | (Band-Independent) Factor |                  |
|---------------------------------------|---------------------------|------------------|
| At solar zenith angle of observations |                           |                  |
| MODIS                                 | 0%                        | 0.35 (0.30–0.37) |
| MISR                                  | 0%                        | 0.23 (0.18–0.25) |
| MODIS+MISR                            | 0%                        | 0.17 (0.13–0.18) |
| MODIS                                 | 50%                       | 0.51 (0.42–0.52) |
| MISR                                  | 50%                       | n/a              |
| MODIS+MISR                            | 50%                       | 0.24 (0.18–0.25) |
| At other solar zenith angles          |                           |                  |
| MODIS                                 | 0%                        | 0.99 (0.28–1.29) |
| MISR                                  | 0%                        | 0.42 (0.24–0.80) |
| MODIS+MISR                            | 0%                        | 0.34 (0.17–0.58) |
| MODIS                                 | 50%                       | 1.40 (0.40–1.82) |
| MISR                                  | 50%                       | n/a              |
| MODIS+MISR                            | 50%                       | 0.48 (0.24–0.82) |

independent of wavelength due to the mathematical form of kernel-based models as long as the weights  $w_l$  used in the inversion are not wavelength-dependent. They depend on the exact location of the angular sampling acquired.

Table IV summarizes noise sensitivities for different sensors and fractions of observations lost due to clouds. Again the cloudy case is not relevant for MISR as this instrument either acquires all observations in a short period of time over cloud-free skies or none at all. The time period used for MODIS is 16 days, and that for MISR 9 days, which are the respective periods used for producing the operational albedo products for each sensor. Clearly, all the retrievals at the mean solar zenith angle of the observations are stable against noise. If the inputs had a random component of, for example, 10% magnitude, the albedos retrieved would only vary by about 2–5%. The error for solar zenith angles other than that of the observations (in this case, for nadir sun and for white-sky albedo) are larger, as expected, amounting to between 0.5–1.0 of the variation in the reflectance observations for the median sensitivity. In the worst cases, retrievals are still stable for scenarios involving MISR, whereas using MODIS alone may in some cases be susceptible to increased noise.

Again, AVHRR or MERIS sampling may be taken to be roughly similar to that seen by MODIS, whereas POLDER sampling will be similar to or better than that seen by MISR when several orbits are used together.

### D. Accuracy of Diffuse Skylight Approximation

In computing the albedo under actual illumination conditions, (32) assumes an isotropic distribution of diffuse skylight.

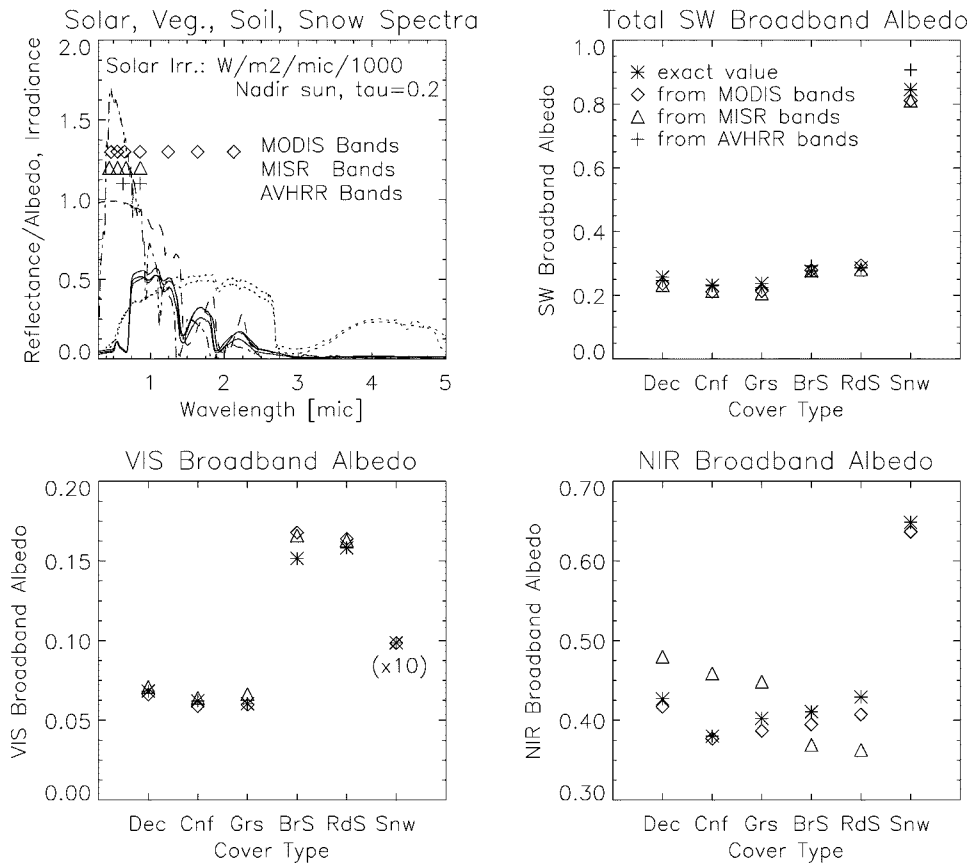


Fig. 8. Upper left: spectra of six different types of landcovers (source: ASTER spectral library, S. J. Hook). These are deciduous tree leaves (Dec), conifer needles (Cnf), and grass (Grs) for vegetation (solid lines), a brown silty loam (BrS), and a dark reddish brown fine sandy loam (RdS) for soils (dotted lines), and fine snow (Snw) for snow/ice (dashed line). Also shown is the solar downwelling spectrum computed with the 6S atmospheric radiative transfer simulation code using a continental aerosol model and a U.S. standard 62 atmosphere (peaked dashed-dotted line). Optical depth at 550 nm was 0.2, the sun was at nadir. Symbols mark the location of the MODIS, MISR, and AVHRR spectral bands. Other panels: comparison of total shortwave, visible and near-infrared broadband albedos computed exactly (stars), and as derived from values at the location of MODIS (diamonds), MISR (triangles), and AVHRR (crosses) spectral bands using conversion coefficients.

This approximation as well as a few others were investigated by Lewis and Barnsley [36]. They find that the approximation is very good, with relative errors generally less than a few percent even in the worst cases, which occur for small solar zenith angles.

#### E. Accuracy of Spectral-to-Broadband Conversion

Six representative spectra taken from the ASTER spectral library were used to investigate spectral-to-broadband conversion. These are three spectra for vegetation (deciduous tree leaves, conifer tree needles, green grass) and three for barren surfaces (brown silty loam, dark reddish brown fine sandy loam, fine snow). Taking these reflectance spectra as an estimate of albedo spectra, which should have very similar properties, exact broadband albedos in the total shortwave (0.3–5.0  $\mu\text{m}$ ), visible (0.3–0.7  $\mu\text{m}$ ) and near-infrared (0.7–5.0  $\mu\text{m}$ ) broadband were computed by convolving with the downwelling solar spectrum. The latter was computed using the 6S code [42], the sun at nadir, a continental aerosol model, and a U.S. standard 62 atmosphere.

Fig. 8 shows the spectra studied and plots the exact broadband albedos for comparison with the values estimated from discrete albedos in satellite spectral bands, the latter derived using

TABLE V  
AVERAGE RELATIVE BROADBAND ALBEDO PREDICTION ERROR AND BEST–WORST RANGE FROM USING NARROW-TO-BROADBAND COEFFICIENTS

| Band   | MODIS      | MISR         | AVHRR     |
|--------|------------|--------------|-----------|
| SW-BB  | 6% (1–10%) | 6% (1–13%)   | 4% (0–7%) |
| VIS-BB | 4% (0–11%) | 5% (3–10%)   | —         |
| NIR-BB | 3% (1–5%)  | 13% (10–21%) | —         |

the conversion coefficients of Table II. Even though vegetation, soils and snow have rather different spectra, results from the MODIS bands are correct to within 10% relative for all surface types and all three broadband. As Table V shows, the mean relative error for the total shortwave, visible and near-infrared broadband albedo is 6, 4, and 3%, respectively.

The corresponding errors when using only the four MISR bands are 6, 5, and 13%. As expected, the near-infrared broadband albedo can be predicted with considerably less reliability from MISR than from MODIS. The error is up to 20% in individual cases. However, this does not strongly impact the accuracy of the total shortwave broadband albedo from MISR due

to the limited contribution of the solar downwelling flux in the near-infrared.

While some published conversion coefficients for the AVHRR red and near-infrared bands produced errors of 15–60% relative, it was surprising that the coefficients given by Brest and Goward [51] for Landsat TM spectral bands produced very good results for the six very different spectra used here and for the corresponding AVHRR bands. The mean error of the total shortwave broadband albedo was only 4%, all estimated albedos being slightly too small. This is excellent given that the spectral sampling for the AVHRR is as sparse as is possible. If confirmed for a larger number of spectra, this bodes well for deriving broadband albedo from the long data record available only from the AVHRR. Also, the conversion coefficients for vegetated surfaces were used throughout. When using the nonvegetated coefficients for the barren surfaces, the results are worse. When using the snow coefficients for the snow case, the result improves.

Required broadband albedo accuracies for climate modeling purposes of 0.05 [22] or 0.02 [9] and [27] are frequently cited. Since the total shortwave broadband albedo of vegetation is about 0.25 and that of moderately bright soils about 0.35, an error of 6% relative in this albedo would provide an accuracy of about 0.02 and hence meet the requirements, although inversion accuracy and noise sensitivity errors will add to this error in the final analysis.

Since spectral-to-broadband conversion is dependent on the spectral distribution of the solar downwelling flux and therefore on atmospheric state, the conversion coefficients listed in Table II are derived for typical or average cases.

#### F. Other Sources of Error

Three other sources of error in albedo retrieval are important but are not treated here, as they either fall outside the scope of this algorithm or require more investigation. The first is the calibration accuracy of the remote sensing instrument. Since albedo is a radiometric quantity, calibration errors will translate directly into albedo errors of a similar magnitude. Calibration of current and future satellite sensors is discussed widely in the literature (e.g., [65]–[67]).

The second is the error incurred in atmospheric correction. This error can mainly be traced to errors in the assumed aerosol optical depth, but aerosol type and properties also play a role [12]. The algorithm discussed here assumes atmospherically corrected reflectances and hence, any errors in these reflectances will be transferred into the derived albedo, generally with a similar magnitude (cf. [7], [8]).

The third effect to be considered is the variability in footprint size that many sensors display, particularly wide-field-of-view sensors [68]. The spatial resolution of a pixel on the edge of the swath is several times coarser than in the center of the swath. When a multiangular series of observations is accumulated over several orbits, data with different ground resolutions are combined. In areas with spatial heterogeneity, this will lead to complex effects that are not well explored, especially not with respect to the impact on BRDF and albedo retrievals. Additionally, issues of geolocation accuracy come into play.

TABLE VI  
COMPARISON OF FIELD-OBSERVED TOTAL SHORTWAVE BROADBAND ALBEDOS WITH SATELLITE-DERIVED VALUES AT JORNADA, NM (USING DATA BY LUCHT *et al.* [69])

| Band   | Observed | Relative Difference |        |
|--------|----------|---------------------|--------|
|        | Value    | AVHRR               | POLDER |
| SW-BB  | 0.221    | 2%                  | 1%     |
| VIS-BB | 0.124    | 3%                  | 7%     |
| NIR-BB | 0.311    | 1%                  | 3%     |

#### G. Albedo Field Validation

A validation study investigating the derivation of broadband albedos from AVHRR and POLDER multiangular observations was carried out at a semidesert site in May 1997 in Jornada, NM, as part of the MODIS land prototyping exercise PROVE'97 [69]. Total shortwave and near-infrared broadband albedos were measured on the ground using upward and downward-looking pyranometers. Visible broadband albedos were inferred mathematically from these measurements.

Data were collected at 44 locations along four 100 m transects radiating away from a tower in a soil-dominated landscape featuring scattered mesquite and yucca bushes and patches of dry senescent grass. Some measurements were also made at a location dominated by the senescent grass. The broadband albedo of the tower site was taken to be well represented by the average of these measurements. Furthermore, the albedo of a square kilometer surrounding the tower was determined by coarsely classifying the area from high-resolution aircraft-acquired imagery and assigning typical albedos to scene components based on findings from the ground observations [69].

Albedos were also derived from the atmospherically corrected multiangular observations acquired by the AVHRR on NOAA-14 and by POLDER during the time period of the field measurements. The Ross-Li BRDF model was inverted to obtain black-sky and white-sky albedo in the red and near-infrared spectral bands. Concurrent AVIRIS spectra were then used to qualitatively extrapolate these measurements over the full spectral range to derive broadband albedos. The AVHRR observations were modeled for the 1.1-km pixel containing the tower, for a block of  $2 \times 2$  pixels, and for an area of  $10 \times 10$  pixels covering the region. The POLDER pixel modeled has a resolution of about 7 km. Albedos were corrected for diffuse skylight using the interpolation method given in this paper. The paper by Lucht *et al.* [69] provides details.

Table VI lists the relative deviation between the ground measurements, the albedos derived from the 1-km AVHRR processing, and those derived from POLDER. The broadband albedos from the space-based sensors are in excellent agreement with those observed on the ground in all three broadband. Only the visible broadband as deduced from POLDER is not in complete agreement with the ground observations, but the spatial scale of the POLDER observations is much larger than the spatial extent of the ground measurements, and the landscape shows some variability on the scale of several hundred meters.

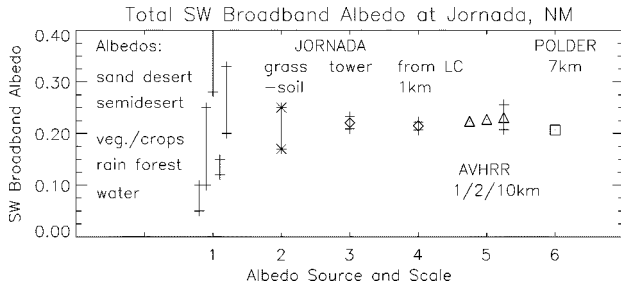


Fig. 9. Field validation of albedo retrieval from space. Column 1 shows possible values of total shortwave broadband albedo for an unknown pixel. Column 2 shows the albedo extremes at a semidesert site (mesquite bush, yucca, dry grass, and soil) at Jornada, NM, based on field measurements made in late May 1997. Column 3 gives the albedo measured at a tower site in form of the average and standard deviation of 100-m long transects leading radially away from the tower (44 measurements). Column 4 gives the albedo found when using albedos measured in the field and applying them to a coarse landcover map of the 1.1-km<sup>2</sup> area surrounding the tower. Column 5 gives three values derived from eight concurrent AVHRR NOAA 14 observations through inversion of the Ross-Li BRDF model and spectral-to-broadband conversion using an AVIRIS spectrum for the site as a qualitative extrapolating function. The three values correspond to scales of 1.1 km<sup>2</sup>, 2.2 km<sup>2</sup>, and the mean and standard deviation of 1.1 km<sup>2</sup> values in an 11 km<sup>2</sup> area, each case containing the tower site. Column 6 shows the albedo derived from concurrent POLDER observations at a scale of 7 km. Adapted from [69].

Fig. 9 graphically compares the results found with the range of possible albedos at the site represented by the scene component albedos, and with the potential albedo of an arbitrary unknown pixel. Clearly, space-based retrieval of broadband albedos from sparse spectral observations following the algorithm given here worked very well for this site.

Albedo validation using airborne multiangle imagery was performed by Lewis *et al.* [70] for a semiarid area in Niger. Data acquired by ASAS were inverted using kernel-driven BRDF models. Broadband albedos were derived from spectral albedos in four bands and coupling with the prevailing atmosphere. Comparison with ground measurements over a millet canopy and for a soil/tiger bush site showed an excellent correlation coefficient of 0.98. On the basis of this validation, spatial maps of albedo were derived for a larger area, demonstrating the algorithm outlined here on airborne data.

## VI. ALGORITHM APPLICATION TO MODIS BRDF/ALBEDO PROCESSING

### A. MODIS Albedo Data Basis and Algorithm

NASA's MODIS sensor is a polar-orbiting across-track scanning spectroradiometer on the EOS-AM platform, called TERRA, with an AVHRR-like swath. Of the 36 spectral bands, it carries seven that are dedicated to the observation of the global land surface in the shortwave optical domain with a spatial resolution of 500 m (250 m for the red and near-infrared bands) [45]. The three greatest expected improvements of MODIS data over AVHRR data with respect to BRDF and albedo retrieval are onboard calibration, accurate geolocation, and routine concurrent characterization of atmospheric parameters.

MODIS data processing will provide both atmospherically corrected reflectances and Ross-Li BRDF/albedo model parameters, allowing us to reconstruct reflectances and albedo for any

TABLE VII  
RELATIVE ERROR (PERCENT) IN REFLECTANCE ( $\rho$ ) AND WHITE-SKY ALBEDO ( $\alpha_{ws}$ ) RETRIEVAL WHEN PERFORMING ATMOSPHERIC CORRECTION USING THE LAMBERTIAN ASSUMPTION AND A ONE-STEP ITERATION LOOP BETWEEN CORRECTION AND BRDF RETRIEVAL. REFLECTANCES  $R$  FOR MODIS+MISR COMBINED ANGULAR SAMPLING, RANGES WITH RESPECT TO DIFFERENT BRDF TYPES AND SAMPLING DISTRIBUTIONS, OPTICAL DEPTH  $\tau$  AT 550 nm (FROM HU *et al.*[8])

| Band                         |     | $\tau = 0.1$ | $\tau = 0.2$ | $\tau = 0.2$ |
|------------------------------|-----|--------------|--------------|--------------|
| <i>Lambertian Assumption</i> |     |              |              |              |
| $\rho$                       | Red | 3.2 (2-8)    | 4.7 (2-12)   | 7.5 (4-18)   |
| $\rho$                       | NIR | 1.9 (1-4)    | 3.1 (2-7)    | 5.0 (3-12)   |
| $\alpha_{ws}$                | Red | 1.1 (0-3)    | 1.5 (0-3)    | 1.8 (0-5)    |
| $\alpha_{ws}$                | NIR | 1.5 (0-3)    | 1.9 (0-3)    | 2.3 (0-5)    |
| <i>One-Step Iteration</i>    |     |              |              |              |
| $\rho$                       | Red | 0.5 (0-2)    | 1.1 (0-4)    | 2.6 (1-9)    |
| $\rho$                       | NIR | 0.2 (0-1)    | 0.5 (0-1)    | 1.3 (0-2)    |
| $\alpha_{ws}$                | Red | 0.4 (0-1)    | 0.7 (0-2)    | 1.3 (0-3)    |
| $\alpha_{ws}$                | NIR | 0.2 (0-0)    | 0.3 (0-1)    | 0.7 (0-2)    |

geometry as standard data products to the user. Atmospheric correction will be achieved with unprecedented quality due to the presence of spectral bands on MODIS, which allow a good characterization of the atmosphere and cloud-clearing. Atmospheric aerosol optical depth, water vapor, and ozone content derived from MODIS will be used in a state-of-the-art algorithm [7] to correct both aerosol and molecular scattering and retrieve the surface reflectance for each observation. The algorithm is also capable of addressing the BRDF-dependent coupling of atmospheric and surface scattering. Table VII summarizes the error potentially made when assuming a Lambertian surface and how this error is reduced if a one-loop iterative retrieval of the surface BRDF is performed [8]. At an aerosol optical depth of 0.2 at 550 nm, the relative reflectance error at MODIS and MISR observation angles is reduced on the average from 3% to less than 1%, and for albedo from 2% to less than 1%. For an optical depth of 0.4, it is reduced from 8% to 3% for reflectance, and from 2% to 1% for albedo.

The MODIS BRDF/albedo standard data product will provide to users the model parameters  $f_k(\Lambda)$ , which are at the heart of the algorithm described here. In its full-up mode, data from two MODIS instruments, one on the EOS-AM and one on the EOS-PM platform, will be merged with MISR (AM platform) data to provide the best angular sampling from EOS instruments. MISR has three visible and one near-infrared band that are similar to MODIS bands [46]. From these data, BRDF and albedo will be derived and stored in form of the coefficients of a kernel-driven BRDF model. Users may then follow the outline given in this paper when they make use of the data product.

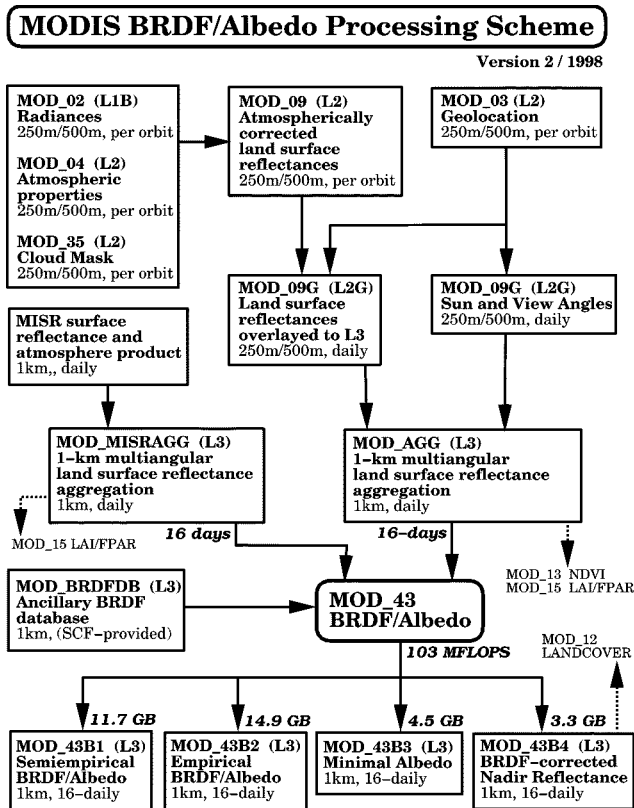


Fig. 10. Processing flow for the MODIS BRDF/albedo algorithm. Atmospherically corrected MODIS (and later MISR) multiangular reflectance observations are aggregated over 16 days onto a geographic grid. The BRDF/albedo process creates four different output products. Abbreviations: MOD\_xx designates MODIS product and process codes, L2 (level 2) refers to data not reprojected from the instrument swath into a geographic grid, L3 (level 3) refers to reprojected data, and SCF stands for a scientific computing facility outside of the processing depicted.

The operational MODIS BRDF/albedo algorithm has been developed over the last several years and has been peer reviewed several times. An algorithm technical basis document [71] and several publications [11], [33], [52], [61] detail the techniques employed for deriving the product. This paper summarizes the at-launch status of the algorithm, updating and superseding the earlier publications. The algorithm flow is summarized in Fig. 10.

The MODIS BRDF/albedo product will be produced by aggregating all available cloud-cleared and atmospherically corrected surface reflectance observations over 16 or 32 days (depending on cloudiness). The spatial resolution will be 1 km. It will be provided in three visible bands (460, 555, and 659 nm) and in four near-infrared bands (865, 1240, 1640, and 2130 nm), from which total shortwave, visible, and near-infrared broadband values will be inferred using the coefficients by Liang *et al.* [37] given in Table II. The code will utilize a combination of least-squares fitting and a weight of determination analysis to determine the model parameters and predict their quality.

It is currently estimated that the code will require about 100 MFlops of sustained computing power over 16 days to produce the product for that period and the global land surface. The operational algorithm makes use of four different external

toolkits that interface with the production system. It employs error tracking and utilizes methods of code optimization.

## B. MODIS BRDF/Albedo Product

The MODIS BRDF/albedo standard data product (called MOD43) will be subdivided into four different components, two full BRDF/albedo products and two ready-to-use utility products.

- 1) The semiempirical Ambrals BRDF/albedo product will supply coefficients for the Ross-Li semiempirical BRDF/albedo model for each global 1-km land pixel in the seven MODIS land bands and the visible, near-infrared and total shortwave broadbands. A full array of per-band quality control information as well as shape factors that give forward-to-nadir and backward-to-nadir modeled reflectance ratios for 30° viewing and 45° solar zenith angle are also carried. The code is capable of running different kernel-driven BRDF models in competition [11], but this feature will not initially be used.
- 2) The empirical modified Walthall BRDF/albedo product is structurally the same as the semiempirical BRDF/albedo product but is based on the empirical modified Walthall BRDF model, which provides a very simple one-line parameterization of multiangular reflectance and is also of the kernel-driven type [19], [38]. Depending on the frequency of user requests, this product may in the future be upgraded to a next generation of BRDF models, while the semiempirical product is continued for time series consistency.
- 3) The minimal albedo product. Since the BRDF/albedo products that carry the full BRDF/albedo information tend to be rather large and contain albedo in a parameterized form, an easy-to-use smaller-volume albedo product is generated, which carries only a subset of the complete albedo and no BRDF information. Black-sky albedo for 45° solar zenith and white-sky albedo are given in four bands (460, 659, 865, and 1640 nm) and the visible and NIR broadbands.
- 4) The BRDF-corrected nadir reflectance product will provide a nadir-view reflectance in all seven bands derived from the semiempirical BRDF modeling product at the median solar zenith angle of observation. Nadir-view nadir-sun reflectance is one of the model parameters in the semiempirical BRDF/albedo product.

File sizes for the four products will be 0.75, 0.93, 0.28, and 0.21 Gb per day for all global land pixels, or 11.7, 14.9, 4.5, and 3.3 Gb per full 16- or 32-day product. Each product will be available in tiles that measure 1200 × 1200 1-km pixels, which are subsets of the integerized sinusoidal grid that is being used as the geographical storage format [68]. All products will be in the HDF format with an EOS enhancement that allows geographical subsetting (HDF-EOS).

## C. Albedo Derivation From Very Sparse Angular Sampling

Realistically, the number of available multiangular observations and their angular range are at times insufficient for a reliable BRDF inversion and albedo derivation. The main reasons

for this are loss of observations to cloud cover, orbital constraints, and the limited length of time for which data should reasonably be aggregated. In fact, where data of the type produced by MODIS or AVHRR are used as the sole data source and are aggregated for two to four weeks, between a third and one half of global pixels are likely affected by insufficient angular sampling [72], [73]. In some regions, as in the tropics, persistent cloud cover will make good angular sampling an occasional event.

Therefore, a back-up algorithm is employed for deriving albedo in a situation of insufficient angular sampling. This algorithm should make full use of the sparse multiangular information that is available. The approach being followed is to constrain the BRDF shape from prior information but to adjust it to match the observations made. If an estimate of the BRDF shape is available in the form of BRDF model parameters  $f'_k$ , then an estimate of the new observed BRDF may be obtained by finding the factor  $q$  that minimizes

$$\begin{aligned} \epsilon^2 &= \sum_l \{ \rho(\theta_l, \vartheta_l, \phi_l) - q R'(\theta_l, \vartheta_l, \phi_l) \}^2 \\ &= \sum_l \left\{ \rho(\theta_l, \vartheta_l, \phi_l) - q \sum_k f'_k K_k(\theta_l, \vartheta_l, \phi_l) \right\}^2 \end{aligned} \quad (47)$$

where  $\rho_l$  are the observed and  $R'_l$  are the reflectances estimated from the *a priori* BRDF model. Minimizing this equation leads to the observation-adjusted new model parameters

$$f_k = q f'_k = \frac{\sum_l \rho(\theta_l, \vartheta_l, \phi_l) R'(\theta_l, \vartheta_l, \phi_l)}{\sum_l R'(\theta_l, \vartheta_l, \phi_l)^2} f'_k \quad (48)$$

where the value of  $q$  should generally not be substantially different from unity.

The basis of this derivation is the assumption that the shape of a given BRDF type approximately scales linearly with the overall reflectance at least over part of the possible reflectance range. In other words, the shape of a BRDF will be linearly more pronounced or less pronounced in proportion to the overall reflectance of the scene. This assumption is certainly not generally valid but will capture a large portion of the effect that is to be modeled. Generally, a dark scene with a low contrast between scene elements will show a relatively weak BRDF, whereas a scene with a stronger contrast between scene elements due to one scene component possessing a larger component signature will produce a stronger shape. As scene properties are assumed to be the same otherwise, the shape of the BRDF's will be similar in a relative sense to the extent that the physics of scattering will not be substantially changed by the difference in brightness. In reality, brighter scenes will lead to more multiple scattering among other effects, but this will usually not be a dominant influence. Some evidence of shape similarity may be seen in Fig. 5, where the solar zenith-angle dependence of a deciduous forest is similar in the red and the near-infrared wavebands in a relative manner, the absolute scales being different in each case. However, this procedure is meant to model small variations in surface brightness from one case to the other, not differences as large as the difference between, e.g., red and near-infrared BRDF's. A different estimated BRDF  $f'_k$  should be used in this

case for each band to be modeled. Most importantly, the estimated BRDF will be scene-dependent (land cover dependent).

If only one observation is used (for example, because the data basis is maximum-value composited), these relationships are reduced to

$$f_k = q f'_k = \frac{\rho(\theta, \vartheta, \phi)}{R'(\theta, \vartheta, \phi)} f'_k \quad (49)$$

that is the parameters, and hence, the reflectances and the albedos as well, are simply scaled by the ratio of observed and *a priori* BRDF model-estimated reflectance at the viewing and illumination geometry of the single observation used [14], [74]. Naturally, using just one observation will be less reliable than using several observations but should still coarsely adjust the BRDF and the albedo to local pixel properties.

In cases where the number of observations available is too small for a full BRDF inversion, the MODIS BRDF product will utilize a global BRDF database to predict a shape type for the BRDF, which will then be adapted to fit the available observations following the procedure given. If no observations are available at all, the database BRDF will be entered into the product unaltered. The heritage of the data given is flagged in each case. The BRDF database will initially be a land cover-derived database where the BRDF's used are field-observed BRDF's adjusted to reflect AVHRR reflectances for each location and season [74]. In the postlaunch period, the database will be iteratively repopulated by MODIS-derived BRDF's.

#### D. BRDF Model Alternatives

From the above discussions, the advantages of using a kernel-based BRDF model should be obvious. A potential not yet realized is that the full and very well developed apparatus of the theory of linear systems could be brought to bear in analyzing the BRDF inversion process with linear models. Advanced treatments are readily available, for example, [75]–[77].

In this paper, the Ross–Li BRDF model was the focus. Alternative kernel-based BRDF models are available. Roujean *et al.* [32] provide a geometric-optical kernel based on rectangular protrusions. This model is being employed by the POLDER project [10]. Chen and Cihlar [78] have expanded this model to include a more prominent hotspot formulation, at the cost of introducing two additional nonlinear parameters that require predetermination in the framework of a linear modeling concept. Wanner *et al.* [33] give formulations for alternate volumetric and geometric kernels, making different assumptions about the canopy modeled. These are less general than the RossThick–LiSparse-R combination, but may be more appropriate for certain types of scenes [52].

The modified Walthall model [19], [38] is a fully empirical kernel-based model. It is interesting because of its one-line mathematical simplicity but has been shown to be less accurate in angular extrapolation under conditions of sparse angular sampling [61]. This is not surprising given the straightforward geometric nature of the empirical terms employed.

However, BRDF models that are not kernel-based are also available. Of these, mainly the three-parameter models are of interest here, as it is doubtful that more than three parameters can be reliably retrieved from space-based remote sensing. The most

important of these is the model employed for the MISR albedo product, a modified version [12] of a semiempirical three-parameter model by Rahman *et al.* [60]. This model is only semi-linear in its modified form and is nonlinear in its original form, which according to Privette *et al.* [62] is the superior form. Several studies [52], [61], [64] have concluded that the modified Rahman model is very comparable to the Ross–Li BRDF model used here, showing similar trends in fitting as well as similar problems. In practical applications, and under sparse angular sampling, the Rahman model may be somewhat more sensitive to changes in angular sampling and occasionally produce unrealistically large albedos, whereas the Ross–Li BRDF model occasionally produces small negative albedos when sampling is insufficient and/or located in unsuitable angular locations. Comparisons of albedos derived for a New England AVHRR and GOES data set (described subsequently) using the Ross–Li model and the modified Rahman model indicate that the latter produces albedos that on average are about 15% (relative) larger than those produced by the former in the red band, a small but systematic difference in absolute terms that should be resolved.

An interesting alternate albedo model that is not built from a BRDF model is given by Dickinson [79] and Briegleb *et al.* [80] which takes the form  $\alpha(\theta) = \alpha(\cos(\theta) = 0.5)(1+v)/(1+2v\cos(\theta))$ , where  $v$  is a parameter controlling the strength of the solar zenith angle dependence.

Overall, the kernel-based BRDF modeling approach is a good approach that offers several computational and mathematical advantages, especially speedy analytical computations, direct linear spatial scaling, and precomputed albedo polynomial parameterization. However, there is an opportunity if not a need, for improving the kernel expressions used. In MODIS processing, advanced kernel expressions could replace the secondary product currently based on the modified Walthall model. In such modeling, the number of three free parameters should perhaps not be exceeded as it is generally believed that more parameters increase problems of kernel interdependence in cases of sparse angular sampling and exceed the information content recoverable from most remotely sensed signals.

### E. MODIS Albedo Prototyping

The MODIS albedo production process was prototyped on a variety of remotely sensed image data sets representing different surface types. These include an arid environment in Niger investigated by Barnsley *et al.* [16], Lewis *et al.* [70], and Lewis and Ruiz de Lope [81], a tropical environment in Amazonian Brazil investigated by Hu *et al.* [82], and a temperate scene in New England, USA, investigated by d'Entremont *et al.* [83]. Analysis includes the normalization of reflectances to nadir view for improved NDVI retrieval, derivation of albedo, and the spatial and temporal mapping of BRDF model parameters. The New England prototyping data set is used here to demonstrate the algorithm.

NOAA-14 AVHRR and GOES-8 Imager data were colocated for a region comprising 160 800 ( $400 \times 402$ ) 1-km pixels over New England for the time period of September 2–18, 1995. The data were carefully calibrated using the most recent available coefficients, georegistered to a 1-km resolution grid

with residuals of 0.4 km and cloud-cleared using a set of eight standard spectral tests on the visible and thermal bands for the AVHRR and temporal differencing on the GOES data. Cloud shadows and pixels adjacent to clouds were also removed. Atmospheric corrections were performed using 6S [42] and concurrent surface visibility observations from several stations. Details on dataset preparation and model inversion are provided by d'Entremont *et al.* [83].

The AVHRR data, having been observed by an across-track scanning polar orbiting radiometer, display almost constant solar zenith angle with the view zenith angle varying from observation to observation. The GOES data, having been acquired by a geostationary satellite, provide reflectances for a constant viewing zenith angle but changing solar zenith and relative azimuth angles. Combined, the data from these two sensors provide sufficient angular sampling for BRDF inversions. Since the GOES Imager only has a visible channel, data could be combined only with the AVHRR visible band, which has sufficiently similar spectral properties for an analysis. Using AVHRR data alone, as for the near-infrared band, leads to gaps in the product due to persistent cloud cover in some areas during the period considered. Here we use the visible (red) band to demonstrate the relationship of the spatial patterns of albedo observed at the nominal scale of 1 km to landscape features. To this end, the Ross–Li BRDF model was inverted for each land pixel of the scene if at least seven multiangular observations were available in the period.

Fig. 11 shows in three panels the black-sky albedo for solar zenith angles of 0, 45, and 70°. The observations from which these albedos were made had solar zenith angles between 40–60°. Therefore, the albedos shown are in part extrapolations of the model to angles that were not sampled. Black-sky albedo at all solar zenith angles is of interest when constructing albedo under diffuse skylight.

The images show, first of all, that the albedos retrieved follow surface features in the area. The bright values on the eastern coast are urban areas (the cities of Boston, Providence, etc.). The greater New York area is also clearly identifiable by its bright reflectance. Bright albedos also occur in the valley of the Connecticut River, along the Hudson River Valley, and in the agricultural region of the Mohawk Valley (center and middle left). Dark albedos are associated with forested areas, such as the Adirondacks (upper left corner) or the Berkshires, between the Hudson and Connecticut River Valleys. Bright linear features relate to major roadways in the region and associated development. These general regions may also be delineated using Fig. 12, which shows the traditionally computed maximum-value NDVI of the scene and a coarse unsupervised classification of this NDVI into three major groups. Blue areas are wooded, red areas are wooded but probably more open, and yellow areas are open agricultural fields, grass and urban areas. If the BRDF inversions leading to the albedos in Fig. 11 were unstable, one might expect a noisy appearance of the images. Clearly, this is not the case.

Second, one may observe that the albedo increases as the solar zenith angle grows. This is in accordance with expectations based on field-observed data (e.g., [70], [84], [85]). Land surface albedos are largest for sun positions close to the horizon.



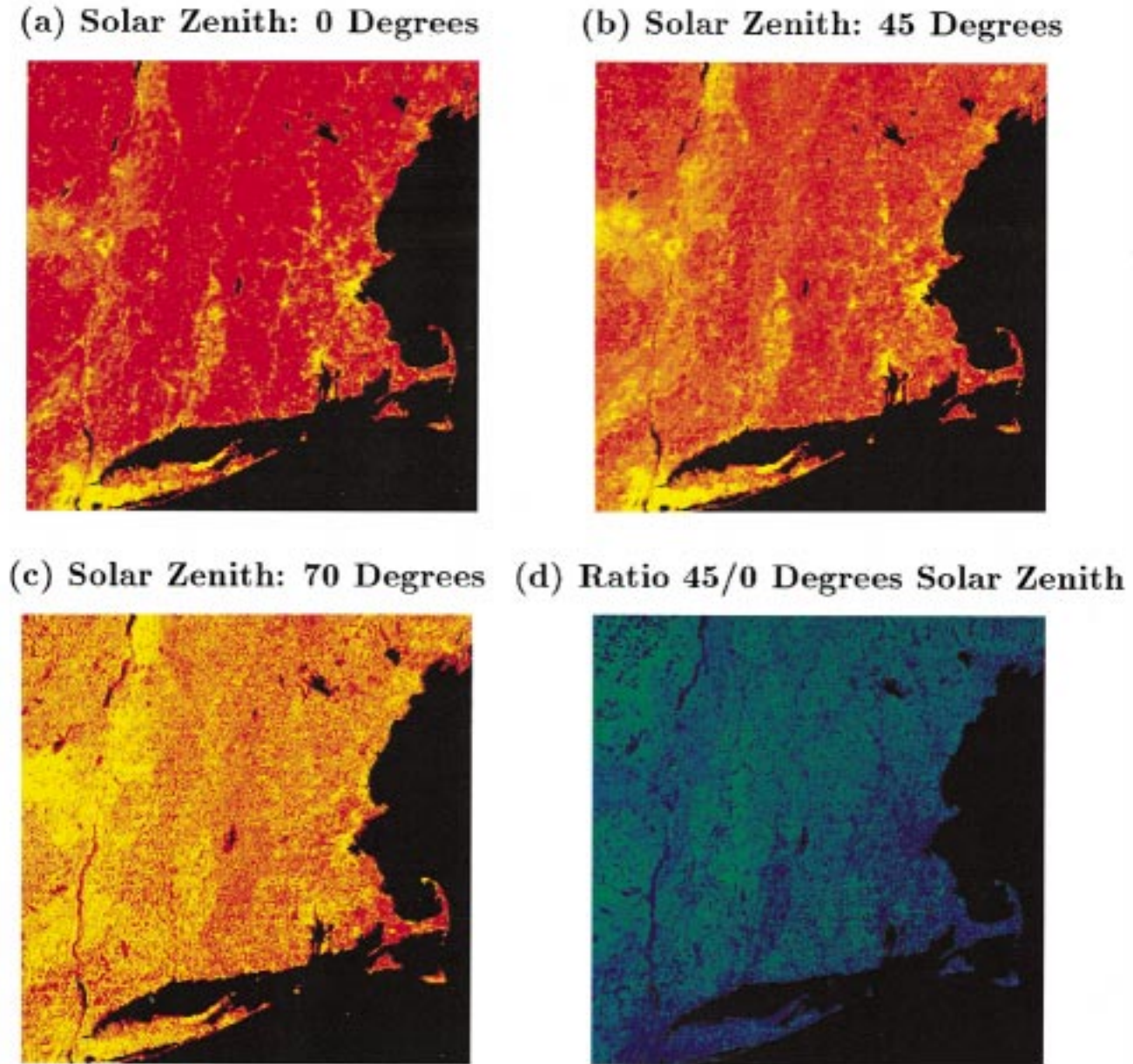


Fig. 11. Black-sky albedo for different solar zenith angles and the ratio of black-sky albedo at solar zenith angles  $45^\circ$  and  $0^\circ$ . Data derived from colocated NOAA AVHRR-14 and GOES-8 Imager data in the red band with a nominal spatial resolution of 1 km. Shown is a  $400 \times 402$  km region of New England from September 2 to 18, 1995. Scaling is from 0 to 0.08 (red to yellow) for black-sky albedos at solar zenith angles  $0^\circ$  and  $45^\circ$  and from 0–0.1 (red to yellow) at solar zenith angle  $70^\circ$ . The ratio image is scaled from 0.8 to 1.8 (blue to green). Albedos are derived from the multiangular observations using the Ross–Li BRDF model. As the solar zenith angle of the observations was mostly between  $40^\circ$  and  $60^\circ$ , some of the images are extrapolated in solar zenith. White-sky albedo is very similar to the black-sky albedo at  $45^\circ$  solar zenith angle. The sun is never at nadir in September in New England, but this illumination condition is relevant for diffuse skylight. The images clearly show major land surface features such as the Hudson, Mohawk, and Connecticut River Valleys, the wooded Berkshire range of hills, and large and small cities throughout the region. The ratio image shows the spatial variation in the solar zenith angle dependence of albedo with region and land cover types. Urban and disrupted areas show a drop of albedo with solar zenith angle due to shadowing, and forested areas show an increase.

Spatial surface albedo contrast, however, is strongest for small solar zenith angles.

Fig. 12 also shows the BRDF-corrected reflectance for nadir viewing and nadir illumination. Again, data are strongly extrapolated in angle. Note that due to kernel normalization this image is identical with a spatial image of the isotropic kernel parameter  $K_{iso}$ . Also shown is the ratio of nadir-view reflectance and black-sky albedo, each computed at  $45^\circ$  solar zenith angle. The variations seen in this ratio demonstrate that the reflectance in a single direction is not a sufficient predictor of albedo, as BRDF

shape varies from one location to the next. Again, landscape features are clearly seen in this image as surface properties determine the relationship between the anisotropic bidirectional reflectance observed and the albedo.

#### F. Biophysical Interpretation

Different surface types display a different solar zenith angle dependence of albedo. This is due to the difference in optical and structural properties between different landcover types, leading to different BRDF's. This is clearly shown in the

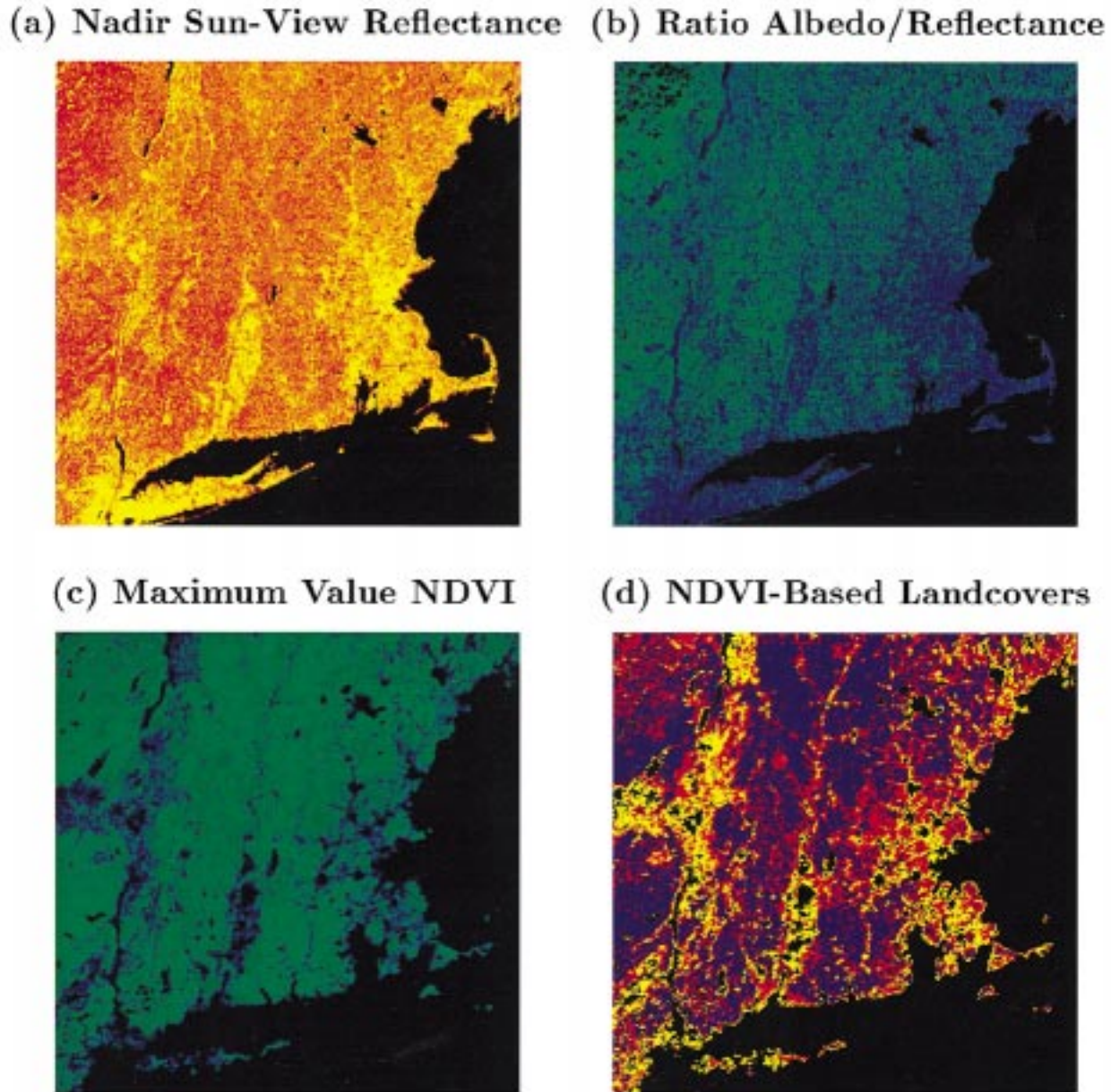


Fig. 12. Satellite data same as in previous figure. (a) BRDF-normalized reflectance for nadir sun and nadir view. This geometry brings out most of the detail of the landscape. Scaling is from 0 to 0.08, (red to yellow) as in the albedo images of the previous figure, (b) ratio of black-sky albedo and BRDF-corrected nadir-view reflectance for  $45^\circ$  solar zenith angle. This image demonstrates that reflectance is not a good predictor of albedo. Scale is 0.8–2.0 (blue to green), (c) maximum value NDVI. Scale is 0.8 to 0.95 (blue to green). Black land areas are those where no cloud-free AVHRR observations were available over the entire period, and (d) three landcover types inferred by unsupervised classification of the maximum value NDVI. Blue and red are forested and may not be substantially different in terms of type, and yellow is suburban and agricultural open space.

lower right panel of Fig. 11, which shows the ratio between the black-sky albedo at  $45^\circ$  and that at  $0^\circ$  solar zenith angle (i.e., the increase or decrease of albedo with solar angle). The ratio is obviously largest for wooded areas and smallest for urban areas, where in some cases, the albedo at  $45^\circ$  may actually be smaller than that at nadir due to strong shadowing within the pixel. This indicates that the solar zenith angle dependence of albedo carries information about the surface. The similarity of the image showing the albedo ratio Fig. 11, with that showing the ratio of reflectance to albedo Fig. 12, shows that both reflect similar aspects of the same basic spatial variation in BRDF shape.

The question of whether there is a semiempirical biophysical interpretation of the Ross–Li BRDF model parameters  $f_k$  is therefore of great interest. The isotropic parameter is equivalent to nadir-view nadir-sun reflectance. The volumetric parameter is in theory exponentially related to leaf area index (LAI), while the geometric parameter is a function of crown/object density and size, related to surface roughness (gapiness of the landscape). Whether empirical transformations between these model parameters and biophysical parameters and based on the variability seen in a given scene and in view of the range of expected values are valid remains to be seen [86]. Roujean *et al.* [34] have explored ideas in this respect, using airborne POLDER data and



inversions of a BRDF kernel-based BRDF model to derive experimentally albedo, vegetation fraction, leaf area index, fraction of absorbed photosynthetically active radiation, and aerodynamic roughness. Disney and Lewis [53] show that the parameters of kernel models may be related to basic vegetation parameters from a systematic analysis using ray-tracing techniques. However, due to the empirical aspects of the semiempirical modeling conducted and problems of kernel coupling for sparse angular sampling, there are likely some limitations of what may be achieved. Use of these models for reconstructive inversion of more physical models at optimal angles is perhaps a promising perspective.

## VII. CONCLUSION

This paper outlines an algorithm for the derivation of land surface albedo from multiangular observations by satellites and explores the potential accuracy of such a technique. The scheme given will be systematically applied to MODIS data for the production of a 1 km MODIS BRDF/albedo standard data product. Evaluation of this product will allow a much improved parameterization of radiometric exchanges at the Earth's surface. Such improvements will benefit a variety of modeling efforts involving radiometric modeling such as studies of biochemical light absorption in plant canopies, evapotranspiration, atmospheric radiative transfer, atmospheric circulation, and cloud formation. Reliable global albedo datasets will also shed interesting light on anthropogenic impacts on land surface reflectivity and the associated climate feedbacks [87], [88]. Another interesting area of study will be the role of albedo in dynamic vegetation reactions to altered climatic states [89].

Deriving albedo at a resolution of 1 km will provide new opportunities to provide the albedo parameters required for global modeling. Only at this resolution can histograms by land cover type, season, and zenith angle be generated that are based on systematic observation of the whole range of global ecosystems and ecoregions. Relying, as in the past, on tabulated albedos of mostly varying quality and provenance applied to a general landcover classification, will no longer be convincing. For example, land cover classifications for the New England region agree in that almost all of the area is classified as forested. Albedos predicted from landcover type would lead to a uniform albedo across most of the scene and not to the detail shown in Figs. 11 and 12. Furthermore, the variation of the albedo with solar zenith angle would be the same everywhere, in contrast to the spatial variability of this dependence seen in the data. Hence, analysis of such fine-resolution albedo data should lead to a very substantial improvement of our knowledge of land surface reflective properties and how they should be accurately summarized for land surface modeling.

The data generated by instruments designed for earth radiation budget studies, such as ERBE or CERES [24], [90], are at a spatial scale (25 km), which is much coarser than that of the heterogeneity of many landscapes. Issues of spatial scaling of surface radiometry and problems of validation of coarse-resolution sensors can only be addressed via fine-resolution albedo observations. Due to the nonlinear nature of land surface physical and biogeochemical processes, parameters should be aver-

aged as late in the processing and modeling as possible. Using coarse resolution data to begin with leads to the earliest averaging possible. In heterogeneous regions, subsequent derivations may be affected by unresolved scaling problems [28]–[30]. Kilometer-resolution albedo data will play an important role in addressing these problems.

It should be realized that albedo is not a linear function of reflectance [47]. Therefore, land cover-type dependent anisotropic correction factors [91] may not be sufficient in many cases. Using the BRDF of each scene is the way forward, as is evident from the processing being undertaken for MODIS, MISR, POLDER, and the AVHRR [10]–[12], [14].

In the next several years, we may expect a rapid increase in our ability to specify and explore the reflectivity of the land surface not just in single directions (for example nadir), but to characterize the anisotropic radiative energy flow in all angular directions through the use of space-derived global albedo databases.

## ACKNOWLEDGMENT

The authors would like to thank their colleagues on the MODIS BRDF/albedo team, especially M. Barnsley, R. d'Entremont, F. Gao, A. Hyman, B. Hu, P. Lewis, J.-P. Muller, N. Strugnell, and T. Tsang for their numerous contributions to this work. They also would like to thank J. Privette, S. Liang, J.-L. Roujean, G. Ye, J. Dekenis, and J. Borak for support, as well as the members of the MODIS land team.

## REFERENCES

- [1] R. E. Dickinson, "Land processes in climate models," *Remote Sens. Environ.*, vol. 51, pp. 27–38, 1995.
- [2] B. M. Lofgren, "Surface albedo-climate feedback simulated using two-way coupling," *J. Clim.*, vol. 8, pp. 2543–2562, 1995.
- [3] Y.-C. Zhang, W. B. Rossow, and A. A. Lacis, "Calculation of surface and top of atmosphere radiative fluxes from physical quantities based on ISCCP data sets—1: Method and sensitivity to input data uncertainties," *J. Geophys. Res.*, vol. 100, pp. 1149–1165, 1995.
- [4] F. E. Nicodemus, J. C. Richmond, J. J. Hsia, I. W. Ginsberg, and T. Limperis, "Geometrical considerations and nomenclature for reflectance," Washington, DC, Nat. Bur. Stand. Rep., NBS MN-160, 1977.
- [5] K. J. Ranson, J. R. Irons, and D. L. Williams, "Multispectral bidirectional reflectance of northern forest canopies with the advanced solid-state array spectroradiometer (ASAS)," *Remote Sens. Environ.*, vol. 47, pp. 276–289, 1994.
- [6] A. A. Abuelgasim and A. H. Strahler, "Modeling bidirectional radiance measurements collected by the advanced solid-state array spectroradiometer (ASAS) over Oregon transect conifer forests," *Remote Sens. Environ.*, vol. 47, pp. 242–260, 1994.
- [7] E. F. Vermote, N. El Saleous, C. O. Justice, Y. F. Kaufman, J. L. Privette, L. Remer, J. C. Roger, and D. Tanre, "Atmospheric correction of visible to middle infrared EOS-MODIS data over land surfaces: Background, operational algorithm, and validation," *J. Geophys. Res.*, vol. 102, pp. 17 131–17 141, 1997.
- [8] B. Hu, W. Lucht, and A. H. Strahler, "The interrelationship of atmospheric correction of reflectances and surface BRDF retrieval: A sensitivity study," *IEEE Trans. Geosci. Remote Sensing*, vol. 36, pp. 724–738, Mar., 1999.
- [9] A. Henderson-Sellers, Z.-L. Zhang, and R. E. Dickinson, "The project for intercomparison of land-surface parameterization schemes," *Bull. Amer. Meteorol. Soc.*, vol. 74, pp. 1335–1349, 1993.
- [10] M. Leroy, J. L. Deuze, F. M. Breon, O. Hauteceur, M. Herman, J. C. Buriez, D. Tanre, S. Bouffies, P. Chazette, and J.-L. Roujean, "Retrieval of atmospheric properties and surface bidirectional reflectances over land from POLDER/ADEOS," *J. Geophys. Res.*, vol. 102, pp. 17 023–17 037, 1997.

- [11] W. Wanner, A. H. Strahler, B. Hu, P. Lewis, J.-P. Muller, X. Li, C. L. Barker Schaaf, and M. J. Barnsley, "Global retrieval of bidirectional reflectance and albedo over land from EOS MODIS and MISR data: Theory and algorithm," *J. Geophys. Res.*, vol. 102, pp. 17 143–17 162, 1997.
- [12] J. V. Martonchik, D. J. Diner, B. Pinty, M. M. Verstraete, R. B. Myneni, Y. Knjazikhin, and H. R. Gordon, "Determination of land and ocean reflective, radiative, and biophysical properties using multiangle imaging," *IEEE Trans. Geosci. Remote Sensing*, vol. 36, pp. 1266–1281, July 1998.
- [13] M. Leroy and J.-L. Roujean, "Sun and view angle corrections on reflectances derived from NOAA/AVHRR data," *IEEE Trans. Geosci. Remote Sensing*, vol. 32, pp. 684–697, May 1994.
- [14] Z. Li, J. Cihlar, X. Zheng, L. Moreau, and H. Ly, "The bidirectional effects of AVHRR measurements over boreal regions," *IEEE Trans. Geosci. Remote Sens.*, vol. 34, pp. 1308–1322, 1996.
- [15] J. L. Privette, W. J. Emery, and D. S. Schimel, "Inversion of a vegetation reflectance model with NOAA AVHRR data," *Remote Sens. Environ.*, vol. 58, pp. 187–200, 1996.
- [16] M. J. Barnsley, D. Allison, and P. Lewis, "On the information content of multiple view angle (MVA) images," *Int. J. Remote Sens.*, vol. 18, pp. 1937–1960, 1997.
- [17] Y. Knjazikhin, J. V. Martonchik, R. B. Myneni, D. J. Diner, and S. W. Running, "Synergistic algorithm for estimating vegetation canopy leaf area index and fraction of absorbed photosynthetically active radiation from MODIS and MISR data," *J. Geophys. Res.*, vol. 103, pp. 32 257–32 276, 1998.
- [18] K. T. Kriebel, "Albedo of vegetated surfaces: Its variability with differing irradiances," *Remote Sens. Environ.*, vol. 8, pp. 283–290, 1979.
- [19] C. L. Walthall, J. M. Norman, J. M. Welles, G. Campbell, and B. L. Blad, "Simple equation to approximate the bidirectional reflectance from vegetation canopies and bare soil surfaces," *Appl. Opt.*, vol. 24, pp. 383–387, 1985.
- [20] K. J. Ranson, J. R. Irons, and C. S. T. Daughtry, "Surface albedo from bidirectional reflectance," *Remote Sens. Environ.*, vol. 35, pp. 201–211, 1991.
- [21] F. Cabot and G. Dedieu, "Surface albedo from space: Coupling bidirectional models and remotely sensed measurements," *J. Geophys. Res.*, vol. 102, pp. 19 645–19 663, 1997.
- [22] A. Henderson-Sellers and M. F. Wilson, "Surface albedo data for climatic modeling," *Rev. Geophys. Space Phys.*, vol. 21, pp. 1743–1778, 1983.
- [23] J. F. Gewelyn and H. J. Preuss, "A new data set of satellite-derived surface albedo values for operational use at ECMWF," *Arch. Meteorol. Geophys. Bioclim.*, vol. A32, pp. 353–359, 1983.
- [24] Z. Li and L. Garand, "Estimation of surface albedo from space: A parameterization for global application," *J. Geophys. Res.*, vol. 99, pp. 8335–8350, 1994.
- [25] M. Claussen, U. Lohmann, E. Roeckner, and U. Schulzweida, "A global set of land surface parameters," Max-Planck-Inst. Meteorol., Hamburg, Germany, Tech. Rep. 135, 1994.
- [26] J. L. Dorman and P. J. Sellers, "A global climatology of albedo, roughness length and stomatal resistance for atmospheric general circulation models as represented by the simple biosphere model (SiB)," *J. Appl. Meteorol.*, vol. 28, pp. 833–855, 1989.
- [27] P. J. Sellers, "Remote sensing of the land surface for studies of global change," NASA/GSFC Int. Satellite Land Surface Climatol. Proj. Tech. Rep., Columbia, MD, 1993.
- [28] D. S. Kimes, A. G. Kerber, and P. J. Sellers, "Spatial averaging errors in creating hemispherical reflectance (albedo) maps from directional data," *Remote Sens. Environ.*, vol. 45, pp. 85–94, 1993.
- [29] G. B. Bonan, D. Pollard, and S. L. Thompson, "Influence of subgrid-scale heterogeneity in leaf area index, stomatal resistance, and soil moisture on grid-scale land-atmosphere interactions," *J. Clim.*, vol. 6, pp. 1882–1897, 1993.
- [30] W. J. Shuttleworth, Z.-L. Yang, and M. A. Arain, "Aggregation rules for surface parameters in global models," *Hydrol. Earth Syst. Sci.*, vol. 2, pp. 217–226, 1997.
- [31] F. G. Hall, J. R. Townshend, and E. T. Engman, "Status of remote sensing algorithms for estimation of land surface state parameters," *Remote Sens. Environ.*, vol. 51, pp. 138–156, 1995.
- [32] J.-L. Roujean, M. Leroy, and P. Y. Deschamps, "A bidirectional reflectance model of the Earth's surface for the correction of remote sensing data," *J. Geophys. Res.*, vol. 97, pp. 20 455–20 468, 1992.
- [33] W. Wanner, X. Li, and A. H. Strahler, "On the derivation of kernels for kernel-driven models of bidirectional reflectance," *J. Geophys. Res.*, vol. 100, pp. 21 077–21 090, 1995.
- [34] J.-L. Roujean, D. Tanre, F.-M. Breon, and J.-L. Deuze, "Retrieval of land surface parameters from airborne POLDER bidirectional reflectance distribution function during HAPEX-Sahel," *J. Geophys. Res.*, vol. 102, pp. 11 201–11 218, 1997.
- [35] P. Lewis, "The utility of kernel-driven BRDF models in global BRDF and albedo studies," in *Proc. Int. Geosci. Remote Sensing Symp. '95*, Florence, Italy, pp. 1186–1187.
- [36] P. Lewis and M. J. Barnsley, "Influence of the sky radiance distribution on various formulations of the earth surface albedo," in *Proc. Conf. Physics, Measures, and Signals*, Val d'Isere, France, 1994, pp. 707–715.
- [37] S. Liang, A. H. Strahler, and C. W. Walthall, "Retrieval of land surface albedo from satellite observations: A simulation study," *J. Appl. Meteorol.*, vol. 38, pp. 712–725, 1999.
- [38] T. Nilsson and A. Kuusk, "A reflectance model for the homogeneous plant canopy and its inversion," *Remote Sens. Environ.*, vol. 27, pp. 157–167, 1989.
- [39] J. K. Ross, *The Radiation Regime and Architecture of Plant Stands*, W. Junk, Ed. Norwell, MA: Artech House, 1981, p. 392.
- [40] X. Li and A. H. Strahler, "Geometric-optical bidirectional reflectance modeling of the discrete crown vegetation canopy: Effect of crown shape and mutual shadowing," *IEEE Trans. Geosci. Remote Sensing*, vol. 30, pp. 276–292, Jan. 1992.
- [41] R. T. Pinker and I. Laszlo, "Modeling surface solar irradiance for satellite applications on a global scale," *J. Appl. Meteorol.*, vol. 31, pp. 194–211, 1992.
- [42] E. F. Vermote, D. Tanre, J. L. Deuze, M. Herman, and J. J. Morcrette, "Second simulation of the satellite signal in the solar spectrum: An overview," *IEEE Trans. Geosci. Remote Sensing*, vol. 35, pp. 675–686, May 1997b.
- [43] H. A. McCartney, "Spectral distribution of solar radiation—II: Global and diffuse," *Quart. J. Roy. Meteorol. Soc.*, vol. 104, pp. 911–926, 1978.
- [44] A. Kuusk, "A multispectral canopy reflectance model," in *Proc. Conf. Physics, Measures, and Signals*, Val d'Isere, France, 1994, pp. 691–698.
- [45] C. O. Justice, E. Vermote, J. R. G. Townshend, R. DeFries, D. P. Roy, D. K. Hall, V. V. Salomonson, J. L. Privette, G. Riggs, A. Strahler, W. Lucht, R. B. Myneni, Y. Knjazikhin, S. W. Running, R. R. Nemani, Z. Wan, A. R. Huete, W. van Leeuwen, R. E. Wolfe, L. Giglio, J.-P. Muller, P. Lewis, and M. J. Barnsley, "The moderate resolution imaging spectroradiometer (MODIS): Land remote sensing for global change research," *IEEE Trans. Geosci. Remote Sensing*, vol. 36, pp. 1228–1249, July 1998.
- [46] D. J. Diner, J. C. Beckert, T. H. Reilly, C. J. Bruegge, J. E. Conel, R. A. Kahn, J. V. Martonchik, T. P. Ackerman, R. Davies, S. A. W. Gerstl, H. R. Gordon, J.-P. Muller, R. B. Myneni, P. J. Sellers, B. Pinty, and M. M. Verstraete, "Multi-angle imaging spectroradiometer (MISR) instrument description and experiment overview," *IEEE Trans. Geosci. Remote Sensing*, vol. 36, pp. 1072–1087, 1998.
- [47] D. L. Toll, D. Shirey, and D. S. Kimes, "NOAA AVHRR land surface albedo algorithm development," *Int. J. Remote Sensing*, vol. 18, pp. 3761–3796, 1997.
- [48] J. E. Wydick, P. A. Davis, and A. Gruber, "Estimation of broadband planetary albedo from operational narrowband satellite measurements," U.S. Dept. Commerce, Washington, DC, NOAA Tech. Rep., 1987.
- [49] G. Gutman, "A simple method for estimating monthly mean albedo of land surfaces from AVHRR data," *J. Appl. Meteorol.*, vol. 27, pp. 973–988, 1988.
- [50] Z. Li and H. G. Leighton, "Narrowband to broadband conversion with spatially autocorrelated reflectance measurements," *J. Appl. Meteorol.*, vol. 31, pp. 421–432, 1992.
- [51] C. L. Brest and S. N. Goward, "Deriving surface albedo measurements from narrow band satellite data," *Int. J. Remote Sensing*, vol. 8, pp. 351–367, 1987.
- [52] B. Hu, W. Lucht, X. Li, and A. H. Strahler, "Validation of kernel-driven models for global modeling of bidirectional reflectance," *Remote Sens. Environ.*, vol. 62, pp. 201–214, 1997.
- [53] M. Disney and P. Lewis, "An investigation of how linear BRDF models deal with the complex scattering processes encountered in a real canopy. presented at *Proc. Int. Geoscience and Remote Sensing Symp. '98* [CD-ROM].
- [54] D. W. Deering and P. Leone, "A sphere-scanning radiometer for rapid directional measurements of sky and ground reflectance," *Remote Sens. Environ.*, vol. 19, pp. 1–24, 1986.
- [55] D. W. Deering, E. M. Middleton, J. R. Irons, B. L. Blad, E. A. Walter-Shea, C. J. Hays, C. Walthall, T. F. Eck, S. P. Ahmad, and B. P. Banerjee, "Prairie grassland bidirectional reflectance measured by different instruments at the FIFE site," *J. Geophys. Res.*, vol. 97, pp. 18 887–18 903, 1992.

- [56] D. W. Deering, E. M. Middleton, and T. F. Eck, "Reflectance anisotropy for a spruce-hemlock canopy," *Remote Sens. Environ.*, vol. 47, pp. 242–260, 1994.
- [57] D. S. Kimes, "Dynamics of directional reflectance factor distribution for vegetation canopies," *Appl. Opt.*, vol. 22, pp. 1364–1372, 1983.
- [58] D. S. Kimes, W. W. Newcomb, C. J. Tucker, I. S. Zonneveldt, W. van Wijngaarden, J. de Leeuw, and G. F. Epema, "Directional reflectance factor distributions for cover types of Northern Africa," *Remote Sens. Environ.*, vol. 18, pp. 1–19, 1985.
- [59] D. S. Kimes, W. W. Newcomb, R. F. Nelson, and J. B. Schutt, "Directional reflectance distributions of a hardwood and a pine forest canopy," *IEEE Trans. Geosci. Remote Sensing*, vol. 24, pp. 281–293, Jan. 1986.
- [60] H. Rahman, B. Pinty, and M. M. Verstraete, "Coupled surface-atmosphere reflectance (CSAR) model—2: Semiempirical surface model usable with NOAA advanced very high resolution radiometer data," *J. Geophys. Res.*, vol. 98, pp. 20 791–20 801, 1993.
- [61] W. Lucht, "Expected retrieval accuracies of bidirectional reflectance and albedo from EOS-MODIS and MISR angular sampling," *J. Geophys. Res.*, vol. 103, pp. 8763–8778, 1998.
- [62] J. L. Privette, T. F. Eck, and D. W. Deering, "Estimating spectral albedo and nadir reflectance through inversion of simple BRDF models with AVHRR/MODIS-like data," *J. Geophys. Res.*, vol. 102, pp. 29 529–29 542, 1997.
- [63] R. B. Myneni, G. Asrar, and F. G. Hall, "A three-dimensional radiative transfer model for optical remote sensing of vegetated land surfaces," *Remote Sens. Environ.*, vol. 41, pp. 105–121, 1992.
- [64] W. Lucht and P. Lewis, "Theoretical noise sensitivity of BRDF and albedo retrieval from the EOS-MODIS and MISR sensors with respect to angular sampling," *Int. J. Remote Sensing*, vol. 21, pp. 81–98, 2000.
- [65] C. R. N. Rao and J. Chen, "Post-launch calibration of the visible and near-infrared channels of the advanced very high resolution Radiometer on the NOAA-14 spacecraft," *Int. J. Remote Sensing*, vol. 17, pp. 2743–2747, 1996.
- [66] W. L. Barnes, T. S. Pagano, and V. V. Salomonson, "Prelaunch characteristics of the moderate resolution imaging spectroradiometer (MODIS) on EOS-AM1," *IEEE Trans. Geosci. Remote Sensing*, vol. 36, pp. 1088–1100, July 1998.
- [67] C. J. Bruegge, V. G. Duval, N. L. Chrien, R. P. Korechoff, B. J. Geitley, and E. B. Hochberg, "MISR prelaunch instrument calibration and characterization results," *IEEE Trans. Geosci. Remote Sensing*, vol. 36, pp. 1186–1198, July 1998.
- [68] R. E. Wolfe, D. P. Roy, and E. Vermote, "MODIS land data storage, gridding, and compositing methodology: Level 2 grid," *IEEE Trans. Geosci. Remote Sensing*, vol. 36, pp. 1324–1338, July 1998.
- [69] W. Lucht, A. H. Hyman, A. H. Strahler, and M. J. Barnsley, "A comparison of satellite-derived spectral albedos to ground-based broadband albedo measurements modeled to satellite spatial scale for a semi-desert landscape," , submitted for publication.
- [70] P. Lewis, M. I. Disney, M. J. Barnsley, and J.-P. Muller, "Deriving albedo maps for HAPEX-Sahel from ASAS data using kernel-driven BRDF models," *Hydrol. Earth Syst. Sci.*, vol. 3, pp. 1–13, 1999.
- [71] A. H. Strahler, W. Wanner, C. B. Schaaf, X. Li, B. Hu, J.-P. Muller, P. Lewis, and M. J. Barnsley, "MODIS BRDF/albedo product: Algorithm theoretical basis document," NASA EOS-MODIS Doc., Version 4.0, 1996.
- [72] D. P. Wylie and W. P. Menzel, "Two years of cloud cover statistics using VAS," *J. Clim.*, vol. 2, pp. 380–392, 1989.
- [73] D. P. Wylie, W. P. Menzel, H. M. Woolf, and K. I. Strabala, "Four years of global cirrus cloud statistics using HIRS," *J. Clim.*, vol. 7, pp. 1972–1986, 1994.
- [74] N. C. Strugnell and W. Lucht, "Continental-scale albedo inferred from AVHRR data, land cover class and field observations of typical BRDF's," , submitted for publication.
- [75] I. Guttman, *Linear Models: An Introduction*. New York: Wiley, 1982, p. 348.
- [76] R. L. Parker, *Geophysical Inverse Theory*. Princeton, NJ: Princeton Univ. Press, 1994, p. 386.
- [77] C. R. Rao and H. Toutenberg, *Linear Models: Least Squares and Alternatives*. New York: Springer-Verlag, 1995, p. 352.
- [78] J. M. Chen and J. Cihlar, "A hotspot function in a simple bidirectional reflectance model for satellite applications," *J. Geophys. Res.*, vol. 102, pp. 25 907–25 913, 1997.
- [79] R. E. Dickinson, "Land surface processes and climate—Surface albedos and energy balance," *Adv. Geophys.*, vol. 25, pp. 305–353, 1983.
- [80] B. P. Briegleb, P. Minnis, J. T. Suttles, and R. S. Kandel, "Comparison of regional clear-sky albedos inferred from satellite observations and model computations," *J. Clim. Appl. Meteorol.*, vol. 25, pp. 214–226, 1986.
- [81] P. Lewis and E. Vives Ruiz de Lope, "The application of kernel-driven BRDF models and AVHRR data to monitoring land surface dynamics in the Sahel," *J. Remote Sensing*, vol. 1, pp. 155–161, 1997.
- [82] B. Hu, W. Lucht, A. Strahler, C. Schaaf, and M. Smith, "Surface albedos and angle-corrected NDVI from AVHRR observations over South America," *Remote Sens. Environ.*, vol. 71, pp. 119–132, 2000.
- [83] R. E. d'Entremont, C. L. Barker Schaaf, W. Lucht, and A. H. Strahler, "Retrieval of red spectral albedo and bidirectional reflectance from 1-km\*\*2 satellite observations for the New England region," *J. Geophys. Res.*, vol. 104, pp. 6229–6240, 1999.
- [84] P. Minnis, S. Mayor, W. L. Smith, and D. F. Young, "Asymmetry in the diurnal variation of surface albedo," *IEEE Trans. Geosci. Remote Sensing*, vol. 35, pp. 879–891, May 1997.
- [85] I. F. Grant, A. J. Prata, and R. P. Cechet, "The impact of the diurnal variation of albedo on the remote sensing of the daily mean albedo of grassland," , to be published.
- [86] W. Lucht, C. Schaaf, A. H. Strahler, and R. E. d'Entremont, "Remote sensing of albedo using the BRDF in relation to land surface properties," in *Proc. Workshop Optical Remote Sensing of Terrestrial Surfaces*, Tusula, Finland, 1997.
- [87] J. Polcher and K. Laval, "A statistical study of the regional impact of deforestation on climate in the LMD GCM," *Clim. Dynam.*, vol. 10, pp. 205–219, 1994.
- [88] J. Lean and P. R. Rowntree, "Understanding the sensitivity of a GCM simulation of Amazonian deforestation to the specification of vegetation and soil characteristics," *J. Clim.*, vol. 10, pp. 1216–1235, 1997.
- [89] R. A. Betts, P. M. Cox, S. E. Lee, and F. I. Woodward, "Contrasting physiological and structural vegetation feedbacks in climate change simulations," *Nature*, vol. 387, pp. 796–799, 1997.
- [90] B. A. Wielicki, B. R. Barkstrom, B. A. Baum, T. P. Charlock, R. N. Green, D. P. Kratz, R. B. Lee III, P. Minnis, G. L. Smith, T. Wong, D. F. Young, R. D. Cess, J. A. Coakley Jr., D. A. H. Crommelynck, L. Donner, R. Kandel, M. D. King, A. J. Miller, V. Ramanathan, D. A. Randall, L. L. Stowe, and R. M. Welch, "Clouds and the earth's radiant energy system (CERES): Algorithm overview," *IEEE Trans. Geosci. Remote Sensing*, vol. 36, pp. 1127–1141, July 1998.
- [91] R. N. Green and G. L. Smith, "Shortwave shape factor inversion of earth radiation budget observations," *J. Atmos. Sci.*, vol. 48, pp. 390–402, 1991.



**Wolfgang Lucht** (previously Wanner) received the M.Sc. and Ph.D. degrees in physics from the University of Kiel, Kiel, Germany, in 1990 and 1993, respectively.

From 1994 to 1998, he was a Research Associate and then an Assistant Research Professor, Department of Geography and the Center for Remote Sensing, Boston University, Boston, MA. He now is a Researcher with the Potsdam Institute for Climate Impact Research, Potsdam, Germany. He is an Associate Member of NASA's MODIS Science Team, where he has overseen the development and implementation of an algorithm for the operational production of a global 1 km BRDF/albedo data product for MODIS. His research addresses remote sensing data inversion, biogeochemical and radiative vegetation modeling, and the coupling of satellite data with land surface models. As a geographer, he is interested in the perception of landscapes in science, the arts, and politics.



**Crystal Barker Schaaf** (M'92) received the S.B. and S.M. degrees in meteorology from the Massachusetts Institute of Technology, Cambridge, in 1982, the M.L.A. degree in archaeology from Harvard University, Cambridge, in 1988, and the Ph.D. degree in geography from Boston University, Boston, MA, in 1994.

She has been a Research Meteorologist with the USAF Phillips Laboratory, Hanscom, MA, specializing in remote sensing of clouds and the land surface. Currently, she is working as a Research Assistant Professor of Geography at Boston University for NASA's MODIS Project and is involved in land surface algorithm definition for the next generation NPOESS satellite project. Her research interests cover remote sensing of the biosphere and the atmosphere.



**Alan H. Strahler** (M'86) received the B.A. and Ph.D. degrees in geography from Johns Hopkins University, Baltimore, MD, in 1964 and 1969, respectively.

He is currently a Professor of Geography and a Researcher in the Center for Remote Sensing, Boston University, Boston, MA. He has held prior academic positions at Hunter College of the City University of New York, the University of California, Santa Barbara, and at the University of Virginia, Charlottesville. Originally trained as a Biogeographer,

he has been actively involved in remote sensing research since 1978. He has been a Principal Investigator on numerous NASA contracts and grants, and is currently a member of the Science Team for the EOS MODIS instrument. His primary research interests are directed toward modeling the bidirectional reflectance distribution function (BRDF) of discontinuous vegetation covers and retrieving physical parameters describing ground scenes through inversion of BRDF models using directional radiance measurements. He is also interested in the problem of land cover classification using multitemporal, multispectral, multidirectional, and spatial information, as acquired in reflective and emissive imagery of the earth's surface.

Dr. Strahler was awarded the AAG/RSSG Medal for Outstanding Contributions to Remote Sensing in 1993.